RESEARCH ARTICLE

Thalamic deep brain stimulation paradigm to reduce consciousness: Cortico-striatal dynamics implicated in mechanisms of consciousness

Michelle J. Redinbaugh[1]*, **Mohsen Afrasiabi**[1], **Jessica M. Phillips**[1], **Niranjan A. Kambi**[1], **Sounak Mohanta**[1], **Aeyal Raz**[2], **Yuri B. Saalmann**[1,3]*

1 Department of Psychology, University of Wisconsin-Madison, Madison, Wisconsin, United States of America, **2** Department of Anesthesiology, Rambam Health Care Campus, Haifa, Israel; Ruth and Bruce Rappaport Faculty of Medicine, Technion—Israel Institute of Technology, Haifa, Israel, **3** Wisconsin National Primate Research Center, Madison, Wisconsin, United States of America

* saalmann@wisc.edu (YS); mredinbaugh@wisc.edu (MJR)

Abstract

Anesthetic manipulations provide much-needed causal evidence for neural correlates of consciousness, but non-specific drug effects complicate their interpretation. Evidence suggests that thalamic deep brain stimulation (DBS) can either increase or decrease consciousness, depending on the stimulation target and parameters. The putative role of the central lateral thalamus (CL) in consciousness makes it an ideal DBS target to manipulate circuit-level mechanisms in cortico-striato-thalamic (CST) systems, thereby influencing consciousness and related processes. We used multi-microelectrode DBS targeted to CL in macaques while recording from frontal, parietal, and striatal regions. DBS induced episodes of abnormally long, vacant staring with low-frequency oscillations here termed vacant, perturbed consciousness (VPC). DBS modulated VPC likelihood in a frequency-specific manner. VPC events corresponded to decreases in measures of neural complexity (entropy) and integration (Φ^*), proposed indices of consciousness, and substantial changes to communication in CST circuits. During VPC, power spectral density and coherence at low frequencies increased across CST circuits, especially in thalamo-parietal and cortico-striatal pathways. Decreased consciousness and neural integration corresponded to shifts in cortico-striatal network configurations that dissociated parietal and subcortical structures. Overall, the features of VPC and implicated networks were similar to those of absence epilepsy. As this same multi-microelectrode DBS method—but at different stimulation frequencies—can also increase consciousness in anesthetized macaques, it can be used to flexibly address questions of consciousness with limited confounds, as well as inform clinical investigations of other consciousness disorders.

Author summary

Deep brain stimulation (DBS) is an effective treatment for a number of neurological and
psychiatric disorders. Recent evidence shows that thalamic DBS can increase conscious-
ness under general anesthesia, and has the potential to be an effective treatment for disor-
ders of consciousness like coma. However, past studies also imply that thalamic DBS can
decrease consciousness by producing periods of inactivity with vacant staring. In this
study, we use thalamic DBS to induce vacant periods of perturbed consciousness (VPC)
while recording from frontal, parietal and subcortical brain areas. Much of modern
research on consciousness focuses on cortical contributions, debating if frontal or more
posterior areas are more important. We show via machine learning, information theoretic
and functional connectivity measures that VPC involves altered neural communication
between parietal cortex and subcortical regions, challenging a cortico-centric focus. Fur-
ther, these mechanisms resemble those associated with absence epilepsy, suggesting a link
between this disorder of consciousness and VPC. Finally, occurrence of VPC in our study
was stimulation frequency-dependent and influenced by the experimental history of DBS.
This provides insight to mechanisms of thalamic DBS, informative for clinical manipula-
tions of consciousness.

Introduction

Deep brain stimulation (DBS) is a powerful tool to treat severe conditions impervious to other
interventions, yet the mechanisms remain unclear [1]. DBS may lead to neural excitation/inhi-
bition, regularized activity or altered neural communication. Further, effectiveness varies
depending on stimulation location, parameters, and electrode type [2].

Intralaminar thalamic DBS is an effective tool to increase consciousness in minimally con-
scious state patients [3] and anesthetized primates [4,5]. Of the intralaminar nuclei, the central
lateral nucleus (CL) seems the most promising target, with anatomical connectivity well-suited
to modulate consciousness. In addition to thalamocortical interactions, theories of conscious-
ness implicate interactions within and/or between frontal and parietal cortex [6–9]. CL proj-
ects to both areas, providing input to superficial layers, and sharing reciprocal projections with
deep layers [10,11], which have been shown to be critical for consciousness [4,12,13]. CL
receives input from the reticular activating system and projects directly to the basal ganglia
[14,15], serving as both a key input and output of the structure [16]. While the role of the basal
ganglia in consciousness is debated [17–19], the striatum contributes to integrated information
[20], a measure of neural complexity associated with consciousness [6], and contributes
strongly to decoding neural differences between conscious states [20]. Further, the basal gan-
glia are linked to altered consciousness with hallucinogens [21] and are suppressed during gen-
eral anesthesia [22] and absence epilepsy [23,24].

Evidence suggests CL manipulations can bidirectionally influence consciousness. CL
lesions are linked to consciousness disorders, like spatial neglect and coma [25]; and thalamic
DBS in cats has been reported to induce sleep, produce a syndrome of vacant staring with
behavioral arrest, or absence seizures, depending on the DBS method (e.g., stimulation fre-
quency, current amplitude and electrode placement) [26]. In rodents, optogenetic stimulation
of CL at 40Hz or 100Hz can drive arousal and activity in cortico-striatal-thalamic (CST) net-
works during sleep, while 10Hz leads to behavioral arrest [27]. Similarly, using a multi-micro-
electrode stimulation method (rather than applying current via 1–2 large electrode contacts in
conventional DBS) in macaques (Fig 1), we have shown that DBS specific to CL, more than
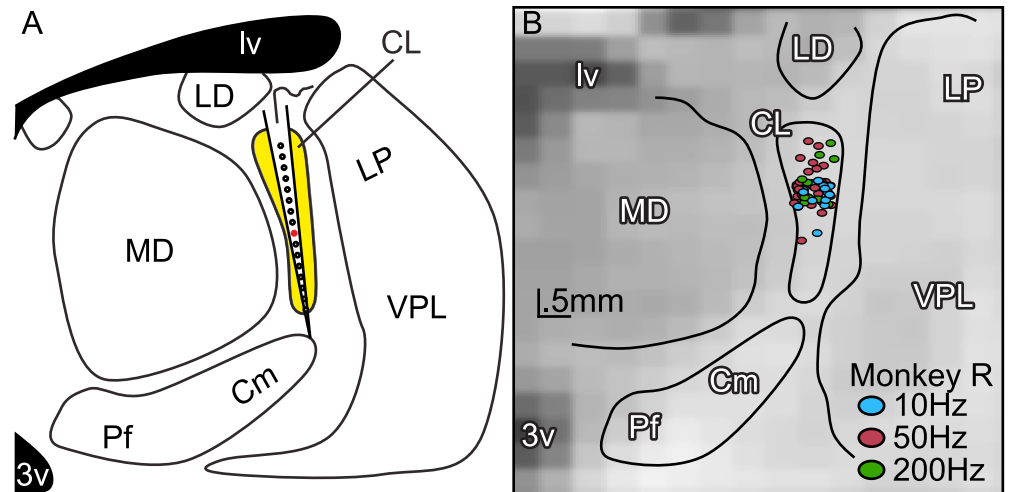
Fig 1. Structural imaging used to target multi-microelectrode DBS to the central lateral thalamus. A: Schematic of coronal thalamic section (right hemisphere) with tailored DBS electrode placed such that contacts span the dorsal-ventral extent of CL (yellow). We simultaneously stimulated via 16 electrode contacts (200μm spacing between contacts), with the centermost contact (contact 8) shown in red. **B:** Track reconstruction of DBS sites overlain on the high-resolution structural image of the thalamus (monkey R, right hemisphere, A8). Only the centermost contact location shown (colored circles) for clarity. For each stimulation, 8 contacts above and 7 contacts below the colored circle would also be stimulated. To improve visualization by reducing overlap, positions plotted with up to 1 voxel (.5mm) jitter separately for 10, 50, and 200Hz experiments. Black lines demarcate different thalamic nuclei: central lateral, CL; centromedian, Cm; lateral dorsal, LD; lateral posterior, LP; mediodorsal, MD; parafascicular, Pf; ventral posterior lateral, VPL. Stimulation performed at all frequencies for most sites.

https://doi.org/10.1371/journal.pcbi.1010294.g001

neighboring thalamic regions, awakens animals from anesthesia when applied at 50Hz, rather than 10Hz or 200Hz [4]. These frequency-specific effects may relate to natural rhythms of CL. In cat [28,29] and monkey [4], a subset of CL neurons exhibit high firing rate (around 50Hz) during wakefulness, but lower firing during sleep and anesthesia. Thus, frequency-specific effects with respect to consciousness may relate to stimulation parameters mimicking these firing patterns [4]. We hypothesize that stimulation frequencies mimicking CL activity patterns during sleep/anesthesia, or inducing abnormal CL activity, will disrupt consciousness in awake, healthy primates.

To test this hypothesis, we used a CL-tailored method of DBS in resting-state (wake) and rewarded (fixation task) conditions while simultaneously recording from frontal cortex, parietal cortex, and striatum of macaques; we also recorded from CL in a DBS-free condition. We applied DBS at different frequencies (10, 50, 200Hz) across a series of stimulation experiments, in addition to experimental series without DBS, to test effect specificity (Fig 2). We predicted that thalamic DBS would cause perturbations in consciousness in a frequency-dependent manner: Stimulations at 50 Hz, mimicking wake-state CL activity patterns, would have little effect on waking behavior; but 10/200Hz DBS (atypical frequencies for wakefulness) would perturb consciousness. Moreover, reduced consciousness would relate to aberrant communication along CST pathways, thought to play a role in consciousness disorders [18,30].

Materials and methods

Ethics statement

All procedures conformed to the National Institutes of Health Guide for the Care and Use of Laboratory Animals and were approved by the University of Wisconsin-Madison Institutional Animal Care and Use Committee (G005777). All surgical and invasive procedures were
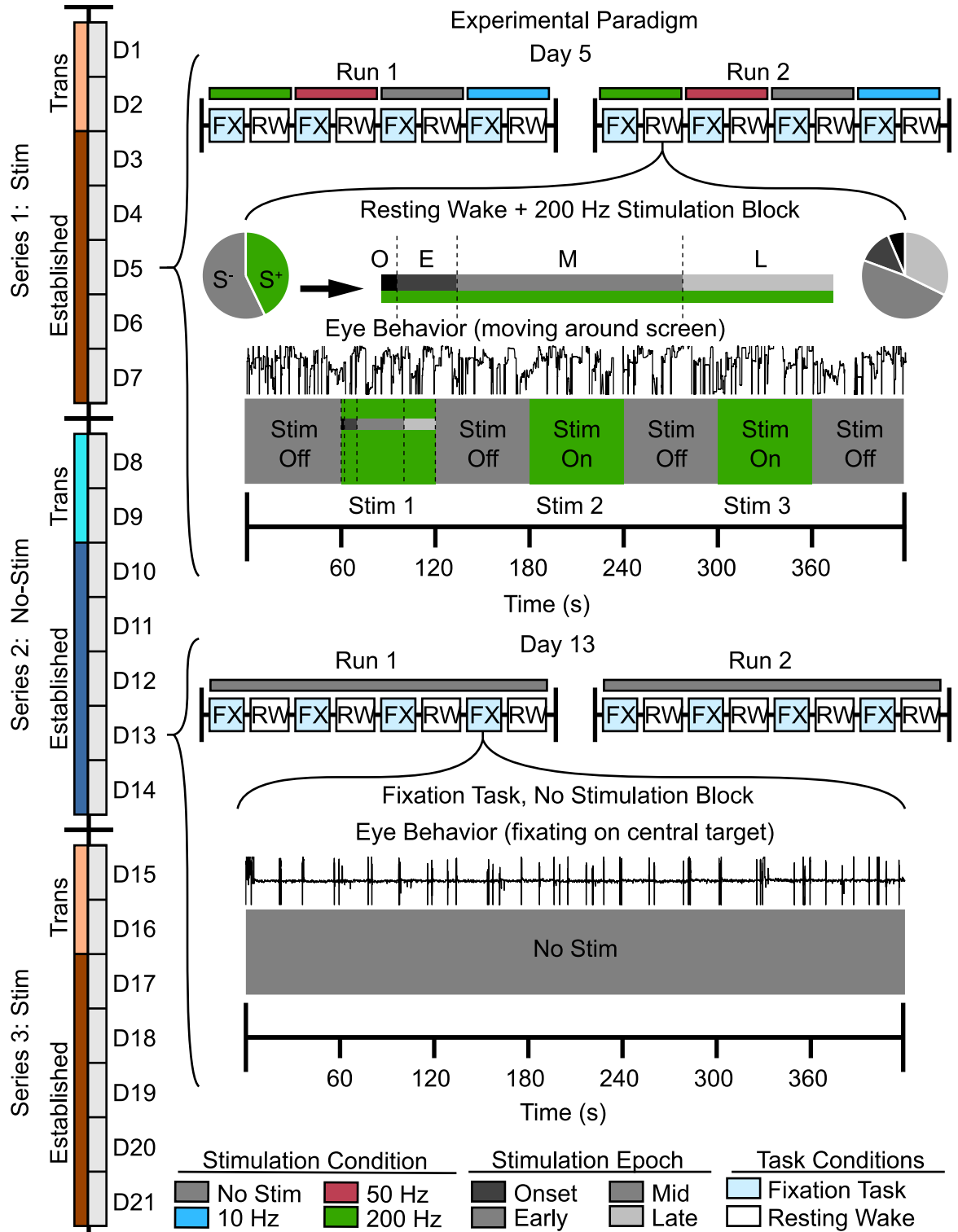
Fig 2. Experimental paradigm for manipulating consciousness in awake macaques. Schematized paradigm to reveal stimulation frequency-specific effects of thalamic DBS across multiple time scales. On the far left, a schematized timeline of the paradigm shown shifting between a series of experiments with (Stim) and without (No-Stim) DBS. The first two recording days of a series were considered transitional, and the following days in the same series were considered established. The top half of the figure presents an example day (D5) in the DBS paradigm, comprised of a pair of experimental runs with pseudorandom stimulation frequency assignment. Here, a sample resting-wake block (420s) using 200Hz DBS is featured, with typical on/off periods (S$^+$/S$^-$) of DBS within the block (60s on, 60s

off). Above the block, one stimulation with duration of 60s is subdivided into shorter time periods: onset (O, 0-2s), early (E, 2-10s), mid (M, 10-40s), and late (L, 40-60s) periods with respect to the start of DBS. The bottom half of the figure presents an example day (D13) in the established No-Stim portion of the paradigm, with a sample fixation task block featured. Here, the eye-tracker trace indicates the animal spends most of the experiment fixating on the central target (centered, steady) as compared to the upper trace where the animal shows typical eye behavior during resting wakefulness (eyes moving around).

performed using sterile techniques. Isoflurane was used for general anesthesia during head implant surgeries and buprenorphine was used for post-operative analgesia. Ketamine and dexmedetomidine were used for anesthesia during minor procedures and meloxicam for analgesia. Animal health and welfare was monitored multiple times daily by experimenters, veterinary and/or animal care staff at the Wisconsin National Primate Research Center.

Model

We acquired data from two male monkeys (*Macaca mulatta*, 4.3–5.5 years old, 7.63–10.30 kg body weight) housed at the Wisconsin National Primate Research Center.

Surgery and electrode placement

We performed a stereotaxic head implant and craniotomy surgery using aseptic techniques under isoflurane general anesthesia (1–2%) according to the procedures described previously [4,20]. We placed 2.5mm craniotomies over the frontal eye fields (FEF), lateral intraparietal area (LIP), CL, and caudate nucleus (CN) using stereotaxic measurements based on high-quality structural MRI acquired in advance of the surgery and comparisons to a stereotaxic atlas [31]. We also acquired MRI subsequent to surgery with electrodes *in situ* to verify electrode placements. We used a GE MR750 3T scanner to acquire 3D T1-weighted structural images from the anesthetized monkeys, with an inversion-recovery prepared gradient echo sequence (FOV = 128 mm^2; matrix = 256 x 256; no. of slices = 166; 0.5 mm isotropic; TR = 9.68 ms; TE = 4.192 ms; flip angle = 12˚; inversion time (TI) = 450 ms). We averaged 6–10 T1-weighted images for the pre-surgery high-quality structural image of each monkey, and we averaged 2 T1-weighted images to visualize electrodes *in situ*. Further imaging details have been described previously [4,20]. Electrode placements were further verified online using functional criteria. Local electrical stimulation at low current in FEF produced eye movements [32], many neurons in the LIP region of interest (ROI) exhibited the classic response characteristic of peri-saccadic activity, and the CL ROI had a subset of neurons with high firing rates around 40-50Hz as previously reported in CL [28]. Finally, we performed post-mortem histology in one monkey, and visualized Hematoxylin and Eosin-stained sections (8 μm) under a microscope, to verify electrode tracks in ROIs.

We separated cortical ROIs into superficial and deep layers using inverse current source density (iCSD) analysis of auditory-evoked ERPs [33]. Both FEF [34–36] and LIP [37,38] have been shown to respond to auditory stimuli. The demarcation between superficial and deep layers was the bottom of the earliest sink after auditory stimulation (approximate boundary between layers 4 and 5). We then assigned electrode contacts to iCSD-defined superficial and deep layers, and confirmed layer assignments using reconstructions of recording sites along each electrode track (computed from electrode depth measurements and MRI of electrodes *in situ*) and spiking activity (demarcating gray from white matter). We used auditory-evoked ERPs to allow comparison of wake data with anesthesia data. CSDs were computed using the CSDplotter toolbox (https://github.com/espenhgn/CSDplotter) for MATLAB (dt = 1 ms, cortical conductivity value = 0.4 S/m, diameter = 0.5 mm). Tones were played in a sequence (200

ms duration; 800 ± 100 ms jitter between tones) comprised of 80% standard tones (0.9 kHz) and 20% deviant/oddball (1 kHz). Further details have been previously described [4].

Electrophysiological recordings and deep brain stimulation

We recorded broadband neural activity (filtered 0.1–7,500Hz, amplified and sampled at 40kHz) using a preamplifier with a high input impedance headstage and OmniPlex data acquisition system controlled by PlexControl software. Probes were MRI-compatible linear microelectrode arrays (MicroProbes) with 16 (FEF and CN) or 24 (LIP and CL) contacts; all were platinum/iridium electrodes 12.5μm in diameter with 200μm spacing between contacts and impedance between 0.8 and 1.0 MΩ. We recorded EEG with titanium skull screws located above dorsal fronto-parietal cortex.

We performed DBS using electrode arrays (24-contacts, 200μm spacing) previously used as recording electrodes, which have reduced impedance. Stimulations (400μs biphasic pulses, negative phase first) occurred simultaneously across the deepest 16 electrode contacts for 60s at 10, 50 or 200Hz with 200μA of current. These parameters had been previously titrated and successfully used to influence consciousness [4,20]. We targeted electrodes to maximize the number of contacts across the dorsal-to-ventral extent of CL (Fig 1), which we have previously shown to optimize stimulation effects [4].

Experimental paradigm

There were 40 total 2–4 hour recording days (18 for monkey R; 22 for monkey W). Monkeys sat upright in a primate chair in a quiet dark room. The animal's head was immobilized using a head post and/or four rods that slid into fabricated hollow slots in the acrylic implant. Each day, we inserted electrodes into ROIs (CL, CN, FEF, and LIP) through chronically implanted guide tubes [4].

We exposed animals to a paradigm that included a series of recording days in which animals received thalamic DBS (Stim) and separate series of recording days in which animals did not receive DBS (No-Stim). The first two days after switching (as well as weekends, when recordings did not take place) between these series types were considered transitional, and all other days in the same series were considered established, as this allowed sufficient data for analysis. Fig 2 depicts the schematized paradigm based on Monkey W. The paradigm was similar for monkey R, but started in the No-Stim condition following previously described anesthetized recordings and DBS experiments [4]. During a non-stimulation series, recordings included 4 brain areas (CL, CN, FEF, LIP). During a stimulation series, we applied DBS through the CL probe, precluding acquisition of CL recordings. On each recording day, monkeys alternated between task-on (rewarded fixation task, "FX") and task-off (resting wake, "RW") blocks. For a stimulation series, each pair of task on/off blocks included thalamic DBS pseudorandomly assigned to one of four conditions (10/50/200 Hz stimulation frequency and No-Stim control). After completing a run of all conditions (8 blocks, i.e., task on/off at 10Hz, 50Hz, 200Hz and No-Stim control), we started another run. Each block of about seven minutes duration included three stimulation replications: typically, stimulations occurred 1–2, 3–4 and 5–6 minutes after the start of the block, with one minute allowed between for recovery. To characterize the timing of observed effects during the 60s stimulations, we considered specific time windows relative to the start of DBS: onset (within 2s of the start of DBS), early (2-10s since start), mid (10-40s since start), and late (40-60s since start). Onset thus described the region of stimulation very close to initiation. In its entirety, this paradigm allowed us to investigate effects at the level of individual stimulations, blocks, recording days, and across the entire history of Stim and No-Stim series including transitions between them.

For the general anesthesia data, we used either isoflurane (0.8–1.5% on 1 L/min O_2 flow; 9 sessions: 5 for Monkey R, 4 for Monkey W) or propofol (0.17–0.33 mg/kg/min i.v.; 9 sessions: 4 for Monkey R, 5 for Monkey W). Full details have been previously described [4].

Behavioral monitoring and video processing

During recordings, experimenters closely observed animal behavior. We monitored eye movements using an eye-tracker and videos focused on the animal's face recorded evidence of facial (mouth and nose) movements and eye openness. Offline, videos were processed using MATLAB and converted into continuous luminance traces based on the average luminance in small windows around the animal's eyes, mouth, and nose. Eye traces revealed periods of open (low luminance) and closed (high luminance) eyes. Derivatives of luminance around the mouth and nose revealed periods when the mouth and nose were moving, or when movement was reduced.

Detecting changes in consciousness

DBS often triggered long-duration periods of behavioral arrest where animals stared vacantly into space and seemed to be unresponsive to their environment. We refer to these as vacant, perturbed consciousness (VPC) events. For systematic detection of VPC, we used custom code identifying periods of time when eye movement was decreased (based on the derivative of the polar coordinates of the eye tracker data), eyes remained open and not partially lidded (based on video eye traces), and facial movement was reduced and/or small and repetitive (based on video mouth and nose traces). Onset times were defined based on when the changes in behavior occurred (stillness and little/no eye movement) and offset was defined by when normal behavior resumed (eye/face/limb movement resumed). Due to technical issues, eye tracker data were not recorded on a subset of VPC events (n = 4), and video data were not recorded on a separate subset (n = 3). Detection was then based on the remaining signals, as well as behavioral notes. Due to the high degree of correlation between these metrics, this did not substantially affect detection. We defined pre- and post-event conditions as the entire time series up to 30s before or after event onset or offset, respectively. We identified possible events as those lasting for longer than 4.2s –the 95% confidence interval of fixation durations in the awake data set, and if the location of the animal's gaze did not match the location of the central fixation target in the fixation task (within 3° of visual angle).

Many states of reduced consciousness including NREM sleep [39,40], general anesthesia [41,42], absence epilepsy [43–46], temporal lobe epilepsy [30,47–49], and coma [50,51] coincide with low-frequency activity in the EEG. Similarly, online, we observed VPC events to coincide with low-frequency EEG activity. To distinguish VPC events from natural long-duration stares (the top 5th percentile), which also showed reduced movement of the face and eyes, we searched offline for evidence of low-frequency activity. Events were assigned as VPC if they involved significant increases at any frequencies 1-9Hz in the EEG (in addition to the behavioral stillness and little/no eye movement) relative to the pre-VPC condition. This frequency range was used to best cover the full range of low-frequency activity observed across different states of reduced consciousness without biasing results towards the assumptions of any one clinical/atypical condition. Automatically detected events that lacked evidence of low-frequency activity were considered to be natural stares and used as the primary control in this study (see below for additional controls), as they shared similarities in behavior to VPC.

Controls

To identify neural correlates of VPC, we compared neural activity during VPC to a variety of controls accounting for activity differences which could be attributed to behavior,

consciousness, or the typical dynamics of wakefulness and attention. To account for time-specific differences, we compared VPC to data recorded up to 30 seconds prior to (Pre) or after (Post) event onset/offset. To account for differences related to consciousness but not behavior per se, we compared VPC to resting wake data, when the animals were conscious but not performing a specific task. Resting data derived from epochs when eye position was stable (for at least 1s), and eyes were open (other face or body movements may have occurred during these windows). The resting state controls were also case-matched (data taken from same recording day with same task, DBS type, and electrode positioning) to account for the experimental paradigm (Stim/No-Stim and stimulation frequency) and electrode positions.

VPC was associated with staring. To account for possible goal-directed fixations, VPC was compared to data from a fixation task, where animals received juice rewards the longer they fixated on a faint, central target. Facial movements were common as animals licked juice rewards. Again, controls were case-matched and we only analyzed data during which the eyes were open and the animal was fixating. The fixation task also allowed comparisons between neural mechanisms present during resting wakefulness and cognitive engagement, which both reflect consciousness. Finally, to account for differences in consciousness while controlling for behavior, we compared VPC to long-duration stares without atypical, low-frequency EEG activity (stare, STR). While these control stares could not be case-matched, as they were rare and occurred randomly in the data set, they could be temporally aligned, similarly to VPC, with a defined onset, offset, pre and post period. This allowed us to compare the temporal dynamics of VPC directly to these specific controls.

Local field potential (LFP) and spike preprocessing

For VPC and stare events, we extracted data up to 30 seconds before behavioral onset (Pre), and up to 30 seconds after offset (Post) when possible. For resting wake controls and the fixation task, we first determined stable eye epochs, to match eye behavior between different conscious states (wakefulness, VPC, general anesthesia). These epochs started 200ms after a saccade and ended 200ms before the next saccade. For all events and controls, we divided epochs of data into non-overlapping 1s windows for analysis, which can be considered similar to trials. For LFPs, we bandpass filtered data from 1-250Hz (Butterworth, order 6, zero-phase filter) and downsampled to 1000Hz sampling frequency. We linearly detrended LFPs, then removed powerline noise (significant sine waves at 60Hz) using the function rmlinesc from the Chronux data analysis toolbox for MATLAB (http://chonux.org/). When individual electrode contacts had signal amplitude greater than 5 standard deviations from the mean of other contacts on the same probe, they were excluded from the analysis. For power spectral density and coherence analyses, we calculated bipolar derivations of the LFPs (the difference between adjacent electrode contacts) to curtail possible effects of a common reference and volume conduction [52–54]. Prior to entropy (H) and Φ^* analyses, we performed ICA (Independent Component Analysis) to minimize the linear dependencies among LFP contacts in each area, then we normalized each LFP to its mean across all epochs for that recording day. We then binarized each LFP with respect to its median amplitude over the 1s epoch, to remove potential biases related to amplitude differences across channels or conditions.

For spiking activity, we bandpass filtered data from 250–5,000 Hz (Butterworth, order 4, zero-phase filter) and sorted spikes using Plexon Offline Sorter software. Spikes were initially detected with thresholds greater than 3 standard deviations from the mean. We used principal components analysis to extract spike shape features and the t-distribution expectation maximization estimation algorithm to determine clusters of spikes with similar features.

During DBS, stimulations induced a brief artifact caused by the applied current. To remove this artifact, we excised a 1ms window around the artifact, linearly interpolated across this window, and removed any significant sine waves at the stimulation frequency using the Chronux function rmlinesc.

Spike rate

We calculated the average spike count across the same 1s windows as the LFP analyses. For epochs that included thalamic DBS, artifact removal decreased the viable window as a function of the stimulation frequency. Thus, the window size was adjusted accordingly and accounted for in the spike rate calculation. For each neuron, spike rate was normalized to data collected during the pre-event condition, to allow comparison with all possible controls. We only analyzed neurons if they were recorded during a VPC or control stare event (in addition to other controls).

Power and coherence spectrograms

For VPC and control stare events, we calculated power spectrograms using 1s sliding windows with 0.1s stride/overlap across the entire time course of the event aligned to the onset of the behavior. Spectrograms were calculated for every bipolar-derived LFP using multi-taper methods (5 Slepian taper functions, time bandwidth product of 3) with the Chronux function mtspecgramc and then averaged across all viable electrode contacts.

To measure the temporal relationship between LFPs, we used coherence within and between CL, CN, FEF and LIP. Coherence is given by:

$$C(f) = \frac{S_{12}(f)}{\sqrt{S_{11}(f) \times S_{22}(f)}} \tag{1}$$

where S(f) is the estimated power spectral density with subscripts 1 and 2 referring to the simultaneously recorded LFPs at two different sites. We applied multi-taper methods (5 Slepian taper functions, time bandwidth product of 3) to yield coherence spectrograms, using the Chronux function cohgramc. For VPC and control stare events, we calculated coherence in 1s sliding windows, stepped 0.1s, for all bipolar-derived LFP pairs corresponding to anatomically plausible pathways. We then averaged coherence values for all LFP pairs representing each pathway.

Φ^* Computation

Integrated Information (Φ) is a proposed index of consciousness measuring both the complexity and integrated structure of a given system [6,55]. While measuring Φ directly is intractable in larger systems [55], surrogate measures such as Φ^*, based on mutual information, have been shown to adequately approximate integrated information and detect changes in consciousness [20,55–58].

We calculated Φ^* [20,55–57] as a practicable estimate of integrated information (Φ). To compute Φ^* based on LFPs, we formed the state of a subsystem (t) at time t (1 ms time bins considering 1 kHz sampling frequency) as:

$$X(t) = \begin{bmatrix} X_{CN}^T(t) & X_{CL}^T(t) & X_F^T(t) & X_L^T(t) \end{bmatrix}$$

where its elements are the bipolar-derived LFP signals, ranging from 1 to 23 signals (resulting from 24 electrode contacts) in each brain area: CN, CL, FEF (F) and LIP (L). The component of $X(t)$ for each area is $N_{ch} \times T$-sized, where N_{ch} specifies the number of bipolar-derived

channels for each of four areas and $T = 1000$ (1s windows, sampled at 1kHz). We next calculated the uncertainty about the states assuming a multivariate Gaussian distribution of the states across time as:

$$p(X) = \frac{1}{((2\pi)^N |\Sigma(X)|)^{1/2}} \exp\left(-\frac{1}{2}(X - \mu(X))^T \Sigma(X)^{-1}(X - \mu(X))\right) \tag{2}$$

where $\Sigma(X)$ (t removed to be concise) is the covariance matrix of X estimated over a 1s data window, $\mu(X)$ is the mean of the state vector X over the window, $|\Sigma(X)|$ is the determinant of the covariance matrix that can be considered a measure of uncertainty about the state X at any time point within the window, and N is the total number of channels across areas. We used the Henze-Zirkler Multivariate Normality test [59] to verify that our states had multivariate Gaussian distributions.

The entropy for the states $X(t)$, given its probability density function (pdf) as $p(X)$, is defined as:

$$H(X) := -\int_{\mathbb{R}^N} p(X) \log(p(X)) \, d^N x \tag{3}$$

The entropy is maximized if (X) is multivariate Gaussian, and can be calculated in closed form as:

$$H(X) = \frac{1}{2}\log(|\Sigma(X)|) + \frac{1}{2}N\log(2\pi e) \tag{4}$$

which can be described as the uncertainty about state $X(t)$ at time t. The mutual information, i.e., the reduction of uncertainty about state (t) at time t, given its past at time $t - \tau$ can be calculated as:

$$I(X_t; X_{t-\tau}) = H(X_t) - H(X_t | X_{t-\tau}) \tag{5}$$

Where $H(X_t | X_{t-\tau})$ is the conditional entropy of state (t) given its past $(t - \tau)$, and can be derived in canonical form with a Gaussian distribution assumption of states as:

$$H(X_t | X_{t-\tau}) = \frac{1}{2}\log(|\Sigma(X_t | X_{t-\tau})|) + \frac{1}{2}n\log(2\pi e) \tag{6}$$

where $\Sigma(X_t | X_{t-\tau})$ is the covariance matrix of the conditional distribution $p(X_t | X_{t-\tau})$ (conditional covariance) that can be expressed analytically as:

$$\Sigma(X_t | X_{t-\tau}) = \Sigma(X_t) - \Sigma(X_t, X_{t-\tau})\Sigma(X_{t-\tau})^{-1}\Sigma(X_t, X_{t-\tau})^T \tag{7}$$

where $\Sigma(X_t | X_{t-\tau})$ is the cross-covariance matrix. Mutual information, I, can be regarded as a measure of the information the current state has about its past, and it is used to calculate Φ^*, a measure of integrated information. Φ^* of the subsystem (t) is information that cannot be partitioned into independent parts of X and can be defined as:

$$\Phi^* = I - I^* \tag{8}$$

Where I^* (disconnected I) is called mismatched information. We calculated I^* for every bipartition of system X. System parts of interest were defined CN, F_s, F_m, F_d, L_s, L_m, L_d; where s, m and d subscripts correspond to superficial, middle and deep layers respectively. Within each cortical layer (F_s, F_d, etc.), there were multiple bipolar-derived channels. We did not partition these individual layers, and so each layer was effectively a subsystem part consisting of multiple parallel channels.

The partition P that minimizes the normalized Φ^* is the *minimum information partition* (*MIP*), as defined in [60]:

$$N_P = (m - 1) \times \min_k \{H(M^k)\} \tag{9}$$

$$MIP = \underset{P}{\operatorname{argmin}} \left\{ \frac{\Phi_P^*}{N_P} \right\} \tag{10}$$

Here m is the number of partitions and M^k is the kth part of subsystem X. N_P counterbalances inevitable asymmetries introduced by computing Φ^* across a number of partitions of unequal sizes. The MIP is the weakest link between the parts of X, where its partition into subsystems results in minimal information loss. We calculated the covariance and cross-covariance matrices for each 1s window using the shrinkage method for a more stable result and averaged them across all windows for each recording day, to calculate the MIP and its corresponding Φ^*, using gradient ascent and L-BFGS optimization method. We incorporated 2 NVIDIA GTX 1080ti GPUs to accelerate the process of searching for the MIP to calculate Φ^*. We calculated I and Φ^* with timelag $\tau = 15$ ms, as this lag maximized Φ^* in our previous study of this same CST system [20].

Φ^* was computed using all available epochs for each condition (pre, post, VPC, control stare, resting wake, and fixation). Because Φ^* is a relative metric that cannot be easily compared between systems with different composition (i.e., different brain areas), we excluded recordings where a given brain region was absent (for example, when no electrode contacts were identified in the deep cortical layers). To account for small differences in Φ^* related to electrode placement, Φ^* was centered relative to the values obtained during recording tasks in the paired fixation experiments. We also computed Φ^* across time for VPC and control stare conditions, aligned to the onset of the event. In this case, Φ^* was normalized (Z score) across all available time and then averaged for VPC and control stare events. For both centered and Z-score values, higher values of Φ^* indicate increased consciousness, while lower values indicate decreased consciousness.

There are other available approximations of integrated information, such as Φ^G. To ensure that our estimates of Φ^* were reliable estimates of integration, we also calculated our effects with Φ^G [61,62]. As we have demonstrated in another paper [20], the effects computed with Φ^* and Φ^G were qualitatively similar. Further, as an additional control, we computed Φ^* after extrapolating the finite sequences into an infinite time series [62–64] to ensure that the finite approximations were not contributing to inaccurate estimates of integration. The effects were qualitatively and statistically similar. This validates that our Φ^* calculations based on 1s epochs were robust.

Machine learning

We computed the power spectrogram of bipolar derived LFPs in 1s epochs (0.5s sliding window) from 11 seconds prior to VPC or control stare onset up to 12 seconds after offset (5 Slepian tapers). Data were only further analyzed between -10.5 to 4.5 seconds (relative to event onset), as this represented the minimum consistent aligned segments across all events. Power values were averaged for each frequency band (delta 1–4 Hz; theta, 4–8 Hz, alpha, 8–15 Hz; beta, 15-30Hz; gamma 30-90Hz) and all contacts in each area of interest (CN, FEFs, FEFd, LIPs, LIPd) which resulted in 25 input features for each 1s time bin.

We trained a Bayesian classifier [65] for each 1s time bin to classify the data into two states: VPC and Control Stare. For the Bayesian classifier, the class-conditional densities were modeled as gaussian distributions with equal covariances. We used an uninformative prior for classes (Normal-Jeffreys prior [66]) to avoid any bias toward any of the classes. Given X as input

feature vector at time t, the posterior probability that the data belongs to class c can be derived as follows:

$$P\{y_t = c|X_t\} = \frac{\exp(\theta_c(X_t))}{\sum_{i=1}^{2} \exp(\theta_i(X_t))} \tag{11}$$

Where $\theta(X_t)$ will be calculated at each time bin t as:

$$\theta_c(X_t) = \mathbf{W}_c^T(t)X_t + w_{c0}(t) \tag{12}$$

$$\mathbf{W}_c^T(t) = \Sigma^{-1}(t)\mu_c(t) \tag{13}$$

$$w_{c0}(t) = -\frac{1}{2}\mu_c^T(t)\Sigma^{-1}(t)\mu_c(t) \tag{14}$$

Where $\mu_c(t)$ is the expected value of class c at time t; and $\Sigma(t)$ is the common covariance matrix for all classes, which is calculated as the unweighted mean of two covariance matrices for two classes and subsequently regularized using shrinkage where the regularization parameter was derived during training and cross-validation. All the parameters in equations above were calculated using the training set at each fold of cross-validation.

We used 10-fold cross validation with 60% of the data as training set and 40% as test set. To test feature importance, we computed Mean Decrease in Accuracy (MDA). One at a time for each feature, we randomly permuted the sample labels (1000 times) and compared average accuracy to that of the unpermuted model. Permutation effectively erases the relationship between the given feature, condition, and other features, and thus the drop in accuracy can be interpreted as the relative importance of the permuted feature [67].

VPC probability and causal power

To compare the relative effects of different stimulation frequencies, we computed VPC and control stare probability by recording block for each condition. To compare DBS effects across longer time scales (different experimental days) we computed VPC and control stare probability in sliding windows (step size = 1 block) consisting of 32 recording blocks (the typical number of blocks recorded in two days). Stimulation predominance (the number of blocks that included thalamic DBS over the 32 recording blocks) was also calculated in each window. Both metrics were normalized to the maximum for correlation analysis.

We computed causal power (CP) [68], for probabilities that represented a theoretical causal structure between a dependent outcome (VPC event) and an independent experimental variable (stimulation frequency). CP is a differential probability ratio indicating the degree to which a proposed cause predicts an outcome more so than alternative causes, and is calculated based on the conditional probability matrix of event (e) co-occurring with/out cause (c), as seen in Eq 15. Positive/negative CP indicates that the probabilistic relationship is causal, and the proposed cause is more/less likely to lead to an event than alternatives.

	Effect Present	Effect Absent
Cause Present	$P(e^+|c^+)$	$P(e-|c^+)$
Cause Absent	$P(e^+|c-)$	$P(e-|c-)$

$$CP = \frac{P(e^+|c^+) - P(e^+|c^-)}{1 - P(e^+|c^-)} \tag{15}$$

Statistical analyses

We performed statistical analyses using correlations and linear mixed effect models in R, the PyMC3 [69] package in Python, and MATLAB. We controlled all p-values (p) using the Holm-Bonferroni method, and report them as p_c when applicable. Models are shown for all interaction tests.

VPC probabilities (with respect to stimulation onset and frequency), causal power, and MIP association probabilities were compared to their generated null-distribution (permutation test, see Fig 3 for an example). We generated distributions (Fig 3A) to represent a given population in our study containing N elements with different member components (for example, N_A, N_B, N_C and N_D could represent the total number of experiments with each stimulation condition (10/50/200Hz and NS control), and n observations (n_A, n_B, n_C and n_D could represent the total number of VPC events observed with each condition). From that distribution, we drew n simulated random samples (Fig 3B), without replacement if the population was finite and unrepeatable, or with replacement if otherwise, from the population, where n = the total number of observations. The process was repeated Nboot times, yielding a distribution of plausible observations under the null hypothesis of the given metric for each member category. Bootstrapping was always performed with replacement. Actual observations were then tested against these distributions to yield Z statistics and p-values (Fig 3C), which were corrected for multiple comparisons. Comparisons of probability (Fig 3D) and sample proportion (Fig 3E), for example, can then be represented across member conditions relative to the null hypothesis, with error bars derived from the standard deviation of null distributions. Note, with this approach, increasing Nboot can increase the goodness of fit between the discrete distributions (Fig 3C, bar histograms) and the fitted distribution (Fig 3C, colored curves). However, the shape of the distribution, and thus the estimated error depends on the dimensions of the source population (N) and the sample rate (n). Because those values match what was done in the study, the resulting error bars reflect a reasonable estimate of the true, expected variance under the null hypothesis and cannot be inflated by Nboot.

To compare *MIPs* across states, we used a kernel density approach to estimate the probability mass functions for each MIP distribution for each state. We then applied a two-sample Kolmogorov-Smirnov test using the Pymc3 package in Python to determine whether these probability mass functions were different. We also compared the probability of different brain areas associating on the same side of the MIP for each state. These probabilities were then compared against the null distribution with 10,000 bootstraps.

We compared EEG power, LFP power, and LFP coherence time-frequency spectrograms between VPC and control stare conditions using the permutest function in MATLAB [70], based on the Maris-Oostenveld method [71]. Tsum statistics, electrode counts, p-values, and bootstrap parameters are reported for significant clusters. We also performed t-tests with multiple comparisons correction at each frequency and time-point, yielding similar results.

To further compare EEG power spectral density between pre, during and post-events, for VPC and control stare conditions, we used paired t-tests at each frequency in MATLAB; p-values were corrected across frequencies. Similarly, we compared Φ^* values across time, with paired t-tests between the bin with maximum Φ^*, and all other time-points; p-values were corrected across time. We evaluated machine learning accuracy using a one-sample
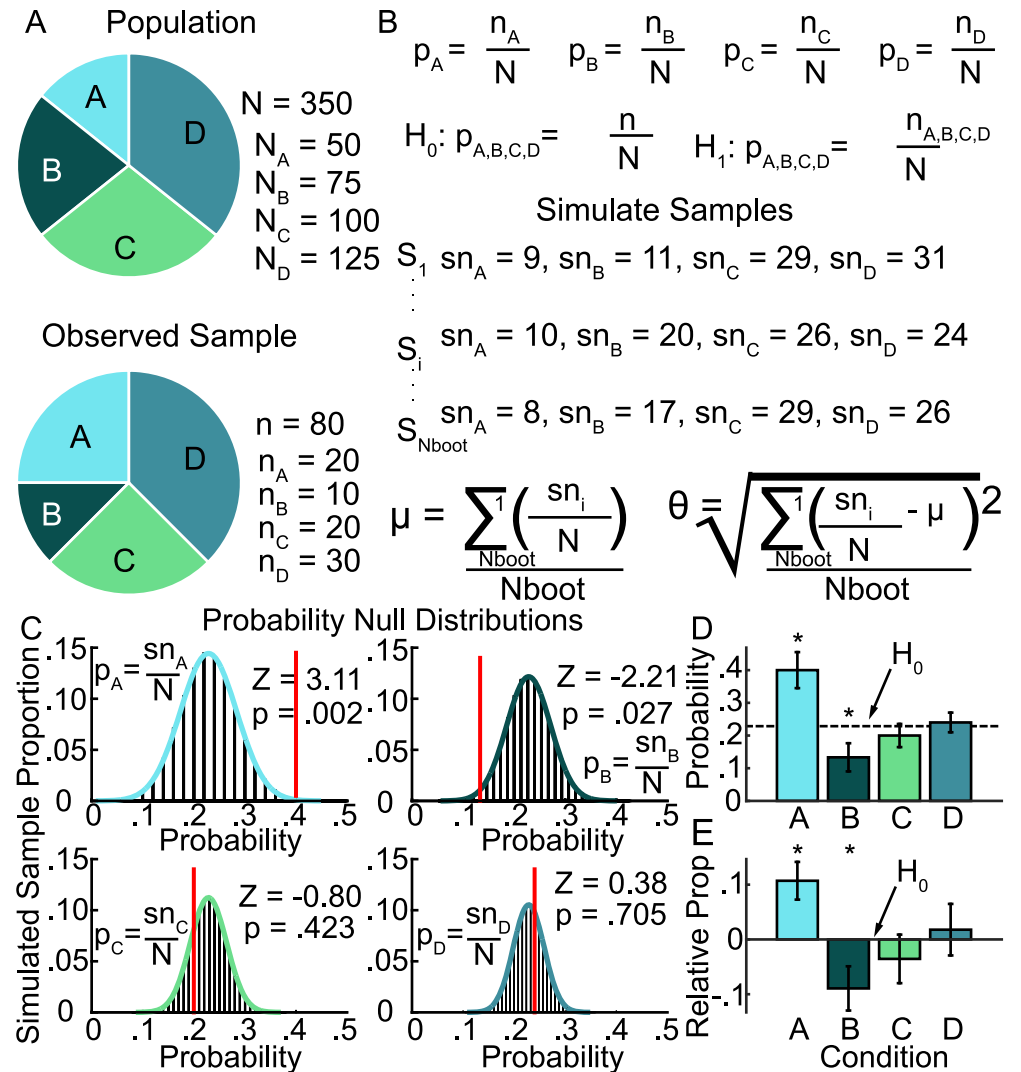
Fig 3. Example of simulated null distribution permutation test for probability analysis. A, Example of hypothetical population, size N, consisting of 4 members and yielding observed sample, size n, consisting of the 4 members. The question to address: Is there category-specific variation in the probability of occurrence for different members of the observed samples? **B,** Equations demonstrating how to represent the question in A as a null hypothesis, and how to simulate samples from the population. **C,** Distributions (histograms) and fitted normal distributions (curves) showing the proportion of simulations yielding a given probability of member occurrence under the null hypothesis. Red lines indicate where the observed sample falls relative to the null distribution, with matching Z statistic and p-value before correction. **D,** Category-specific probability of occurrence where error bars indicate ± 1SD of the null distribution. * indicates statistical significance. **E,** Similar figure to (**D**), but representing the relative proportion of sample occurrences and the null hypothesis that the member proportions observed are the same as those observed in the population.

t-test, comparing results to chance level performance (50%) at each sample across time; p-values were corrected across time.

We compared other effects using linear models (LM in R), reporting t statistics and corrected p-values for all relevant main and interaction effects, or correlations (cor in R), reporting correlation coefficients and p-values. For behavioral changes, we compared data across condition (During versus Pre/Post) for VPC events. For Φ^* controls, we compared data between task condition (resting wakefulness versus fixation task) for all non-stimulation

samples. Statistical analysis was then performed separately for each stimulation condition (10/ 50/200Hz stim-on compared to stim-off). We normalized spike rates to the pre-event condition, then tested with linear models to produce an intercept and p-value. P-values were corrected for all brain regions in the same condition.

For H and Φ^*, we centered values relative to those obtained during fixation controls to account for day-to-day variations. Condition (C, During vs Pre/Post) and event (E, VPC vs control stare) were coded as centered, dichotomous variables. We included animal (A) as a covariate, though similar results were obtained without its inclusion.

$$H, \Phi^* \sim \beta_0 + \beta_1 \times C + \beta_2 \times E + \beta_3 \times C \times E + \beta_4 \times A \qquad \text{(Model 1)}$$

For long-duration stimulation effects, we tested the relationship between local event probability (LEP) and local stimulation predominance (LSP), first using the cor function in R, followed by linear modeling to produce best-fit lines. Both variables were normalized to their maximum, thus ranging between 0 and 1. Comparisons between VPC and control stare conditions used the following interaction model, where event (E) was a centered, dichotomous variable (VPC versus control stare). Animal (A) was included as a covariate, though results were similar either way.

$$LEP \sim \beta_0 + \beta_1 \times LSP + \beta_2 \times E + \beta_3 \times LSP \times E + \beta_4 \times A \qquad \text{(Model 2)}$$

This effect could be simplified by comparing the event probability according to stimulation series type (SS, Stim versus No-Stim). Event (E) was a centered, dichotomous variable (VPC versus control stare); and animal (A) was included as a covariate, though results were similar either way.

$$LEP \sim \beta_0 + \beta_1 \times SS + \beta_2 \times E + \beta_3 \times SS \times E + \beta_4 \times A \qquad \text{(Model 3)}$$

To account for differences seen in the transition between stimulation and non-stimulation series, relative to the established phase, we updated the model to include a 3-way interaction between SS, E, and establishment (EST, Transition versus Established), as a centered, dichotomous variable. Simple effects were consistent between the two models.

$$\begin{aligned} LEP \sim \beta_0 + \beta_1 \times SS + \beta_2 \times E + \beta_3 \times EST + \beta_4 \times SS \times E + \beta_5 EST \times E + \beta_6 SS \times EST \\ + \beta_7 SS \times E \times EST + \beta_8 \times A \qquad \text{(Model 4)} \end{aligned}$$

We compared MDA results along the dimensions of frequency and brain area using a dummy coding approach. Patterns were compared between condition (C, during versus pre) with the following models. P-values were corrected across all frequency and area comparisons.

$$MDA \sim \beta_0 + \beta_1 \times Area + \beta_2 \times C + \beta_3 \times Area \times C \qquad \text{(Model 5)}$$

$$MDA \sim \beta_0 + \beta_1 \times Frequency + \beta_2 \times C + \beta_3 \times Frequency \times C \qquad \text{(Model 6)}$$

Results

Here we first report behavioral and neural measures of perturbed consciousness resulting from thalamic DBS. We call this state vacant perturbed consciousness (VPC). Second, we present evidence that the probability of VPC is modulated by the short- and long-term experimental history of DBS in a frequency-dependent manner (VPC probability higher for 200 and 10Hz cf. 50Hz DBS). Finally, we compare the neural signature of VPC with that in anesthetized states, as well as contrast this signature with that in typical wakeful states, to converge on neural correlates of consciousness.

Thalamic stimulation during wakefulness reduces behavioral and EEG signatures of consciousness

We simultaneously stimulated across the dorsal-ventral extent of CL in awake monkeys via 16 contacts of a linear electrode array (Fig 1). On a subset of recording blocks (17.75% of all non-fixation task blocks, including those with and without stimulation; stimulation frequency- and history-dependence detailed below), animals went from normal behaviors, including scanning the room and making movements with their face and limbs, to suddenly holding their gaze and staring vacantly (Fig 4A). These events occurred without any overt sensory cause, such as a noise that might draw the animal's attention, or visual cue. Animals became still except for occasional small eye flutters and lip movements commonly seen in certain kinds of epilepsies [43–45,72], and would hold their gaze for an abnormally long period of time (> 4.2s, M = 17.64s, SD = 5.96s, 99.93 percentile of all stable fixations which lasted at least 1s). Electrophysiological examination of these events also revealed transient increases in lower frequency (1-9Hz) activity, especially in the EEG. These slower rhythms are commonly associated with reduced consciousness [30,50,73], and below we show corroborating evidence of this. Because the animals also appeared to be staring vacantly into space, we termed this state vacant, perturbed consciousness (VPC).

We detected VPC events (N = 60) based on concurrent changes in behavior and increased low-frequency EEG activity (see Methods). On average, VPC corresponded to substantial reductions in eye movement (Fig 4B, t(55) = 9.05, n = 56, p = 1.75^*10^{-12}, paired t-test), mouth movements (Fig 4D, t(56) = 9.05, n = 57, p = 4.95^*10^{-7}, paired t-test), and nose movements (Fig 4E, t(56) = 4.99, n = 57, p = 6.18^*10^{-6}, paired t-test) relative to pre and post conditions. Eye lids remained open with fewer blinks or changes during VPC compared to pre/post epochs (Fig 4C, t(56) = 13.72, n = 57, p = 2.00^*10^{-16}, paired t-test). During VPC, the EEG showed substantial increases in low frequency power relative to the pre (Fig 4F top, 3–22 Hz, $|t(1798)| \geq 3.43$, n = 1800, $p_c \leq .0465$, paired t-tests) and post condition (Fig 4F top, 6–22 Hz, $|t(1798)| \geq 4.47$, n = 1800, $p_c \leq .0004$, paired t-tests). EEG power prior to and after VPC remained similar (Fig 4F top), except for small differences in the δ band (1–4 Hz, $|t(1798)| \geq 3.69$, n = 1800, $p_c \leq .0204$, paired t-tests). These results cannot be explained by decreased behavioral activity alone. Control stares (STR), behaviorally similar long-duration fixations (N = 64, M = 15.31s, SD = 6.63s, only extreme examples were selected to best match VPC durations) were similar in power relative to pre and post conditions (Fig 4F bottom), except that STR events tended to have lower delta power relative to pre (0–5 Hz, $|t(1918)| \geq 4.05$, n = 1920, $p_c \leq .0046$, paired t-tests) and post (0–7 Hz, $|t(1918)| \geq 4.72$, n = 1920, $p_c \leq .0004$, paired t-tests) conditions. Substantial changes are not present in the EEG between VPC and control stares until around 1.5 seconds after the behavioral onset of an event (Fig 4G), and include significant clusters of increased power only at lower frequencies (δ, θ and α bands, 0–15 Hz, Tsum = 948.889, p = .0130, Nboot = 10,000, permutation test).

VPC corresponds to selective reductions in neural complexity and integration

Measures of complexity are promising neural indicators of consciousness for both animal models and human subjects [20,57,74,75]. We computed entropy (*H*), a measure of the complexity of neural interactions and information-carrying capacity, and Φ^*, which additionally measures integration of network parts, i.e., how partitioning the network influences the generation of information. To assess the relationship between VPC and consciousness, we compared *H* and Φ^* before, during, and after all VPC events and control stares, as well as during resting wake epochs, the fixation task, and two types of general anesthesia (isoflurane and
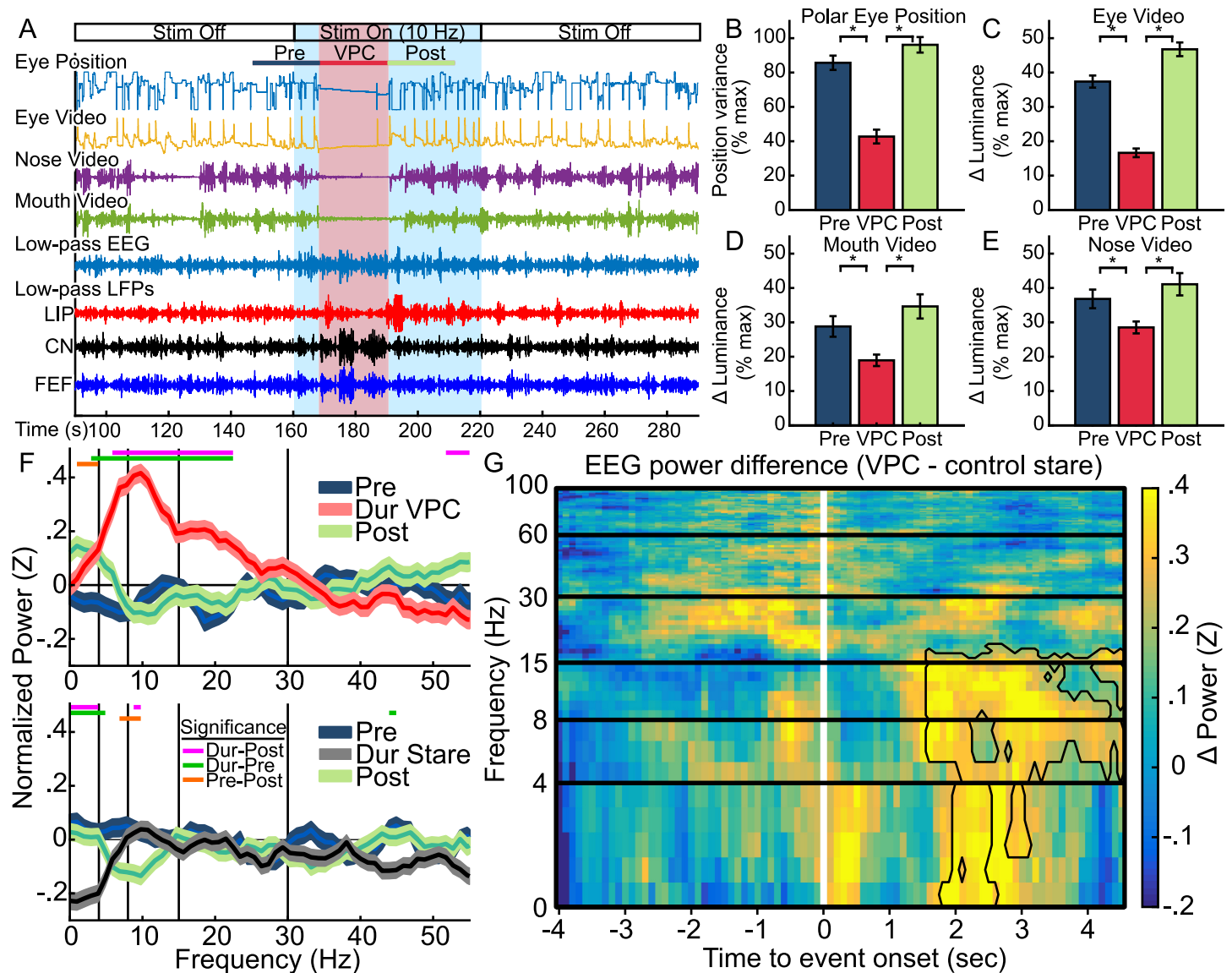
Fig 4. Thalamic DBS triggers periods of behavioral stillness coinciding with low-frequency activity in the EEG, similar to absence epilepsy. A, Example time course of behavioral and neural signatures of a VPC event initiating after 10Hz stimulation. **B,C,D,E,** Average behavioral signatures during VPC relative to pre and post conditions (±SE) for the (**B**) variance in polar eye position from eye tracker, and change in luminance for video data centered on the (**C**) eyes, (**D**) mouth, and (**E**) nose. Luminance changes indicate movement. **F**, Average EEG power (±SE) for VPC and control stares compared to pre and post conditions. Colored straight lines at top indicate regions of significance for t-tests across frequencies comparing spectra from the different conditions. Vertical black lines indicate the cutoff mark of different frequency bands: $\delta = (0, 4)$, $\theta = (4, 8)$, $\alpha = (8, 15)$, $\beta = (15, 30)$, $\gamma_L = (30, 60)$, $\gamma_H = (60, 100)$. **G**, Spectrogram of average differences in normalized EEG power (VPC–control stare) aligned to event onset (white line). Frequency is represented across described power bands. Significant cluster outlined in black.

https://doi.org/10.1371/journal.pcbi.1010294.g004

propofol). We have previously shown that both Φ^* and H tend to be significantly reduced during anesthesia or sleep compared to wakefulness [20]. Relative to the levels recorded during the fixation task, both H (Fig 5A) and Φ^* (Fig 5B) were decreased during VPC, but not control stares, compared to pre and post conditions. The interaction of condition (During vs Pre/Post) and event (VPC vs control stare) was significant for both H (F(295) = 14.578, n = 300, p = 1.64x10^{-4}, ANCOVA) and Φ^* (F(295) = 34.261, n = 300, p = 1.28x10^{-8}, ANCOVA). Differences in Φ^* cannot be explained by general effects of thalamic DBS. When excluding VPC events, there were no significant differences in Φ^* between stim-on (S+) or stim-off (S-)
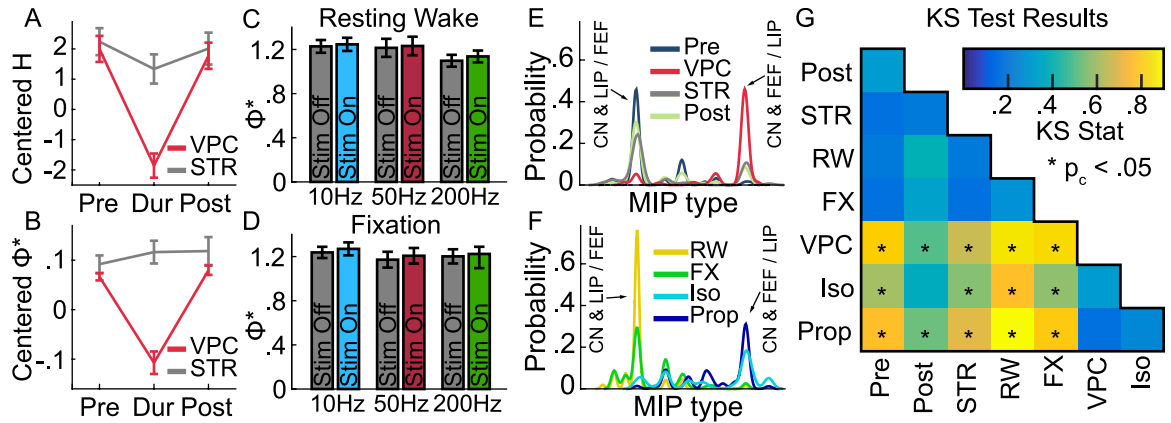
Fig 5. Measure of neural complexity and integration (Φ^*) associated with consciousness selectively decrease during VPC, and integration patterns shift to reflect anesthetized rather than conscious states. A, Average entropy (H) and **B**, Φ^* (±SE) centered relative to the fixation task for VPC and control stares relative to pre and post event conditions. **C, D**, Average Φ^* (±SE) for stim-off (gray bars) and stim-on (colored bars) epochs at different frequencies excluding VPC for resting wake (**C**) and fixation (**D**) controls. **E, F**, Gaussian kernel-density estimates fitted to the probability distribution for the occurrence of different MIP types of the full system for (**E**) pre, VPC, control stare (STR), post, (**F**) resting wake (RW), fixation (FX), isoflurane (Iso), and propofol (Prop) conditions. **G**, Results for the KS tests comparing the MIP kernel-density estimates across all conditions. Color scales with the strength of the KS stat. * indicates corrected p-value (p_c) < .05.

epochs (Fig 5C and 5D) at any stimulation frequency ($t_{50Hz}(62)$ = .29, n = 64, p = .773; $t_{10Hz}(88)$ = .65, n = 90, p = .517; $t_{200Hz}(114)$ = .732, n = 116, p = .466, paired t-tests). Φ^* also proved statistically similar between resting wake and on-task fixation conditions (Fig 5C and 5D, t(118) = 0.925, n = 120, p = .357, paired t-test), meaning decreases in Φ^* were selective to VPC. These results support the conclusion that decreases in Φ^* during VPC events indicate an event-specific reduction in information capacity, complexity and integration associated with consciousness.

Changes in consciousness correspond to changes in cortico-striatal associations

Calculating Φ^* requires computing the minimum information partition (MIP), the cut in the system resulting in the minimum amount of information loss. This indicates system parts which are most integrated. We compared the distribution of MIPs for the largest consistent subsystem (containing CN, layers of frontal and/or parietal cortex) across different states of consciousness (isoflurane/propofol anesthesia, resting wake, fixation, pre/post/during VPC and control stares) using kernel density estimates and two-sample Kolmogorov–Smirnov tests (Fig 5E, 5F and 5G). The results revealed that VPC events exhibit a substantially different MIP distribution relative to pre (KS(28) = 0.80, n = 30, p_c = 1.10x10^{-10}, KS-test) and post (KS(28) = 0.50, n = 30, p_c = 0.0012, KS-test) conditions, while control stare events did not. VPC distributions were clearly different from control stares (KS(28) = 0.65, n = 30, p_c = 9.63x10^{-7}, KS-test), as well as resting wakefulness (KS(28) = 0.85, n = 30, p_c = 3.70x10^{-12}, KS-test), and the fixation task (KS(28) = 0.83, n = 30, p_c = 2.06x10^{-11}, KS-test). But VPC distributions were similar to distributions under isoflurane (KS(28) = 0.3, n = 30, p_c = .8195, KS-test) and propofol (KS(28) = 0.18, n = 30, p_c = 1, KS-test) anesthesia. See Fig 5G for full KS-test comparisons. This shows that the network is reconfigured in the same way for VPC as for general anesthesia.

To further interrogate this effect, we used the MIP distributions to determine the probability of different areas associating on the same side of the MIP as a measure of connection strength (Fig 6A and 6B). While cortical connections remained relatively consistent across
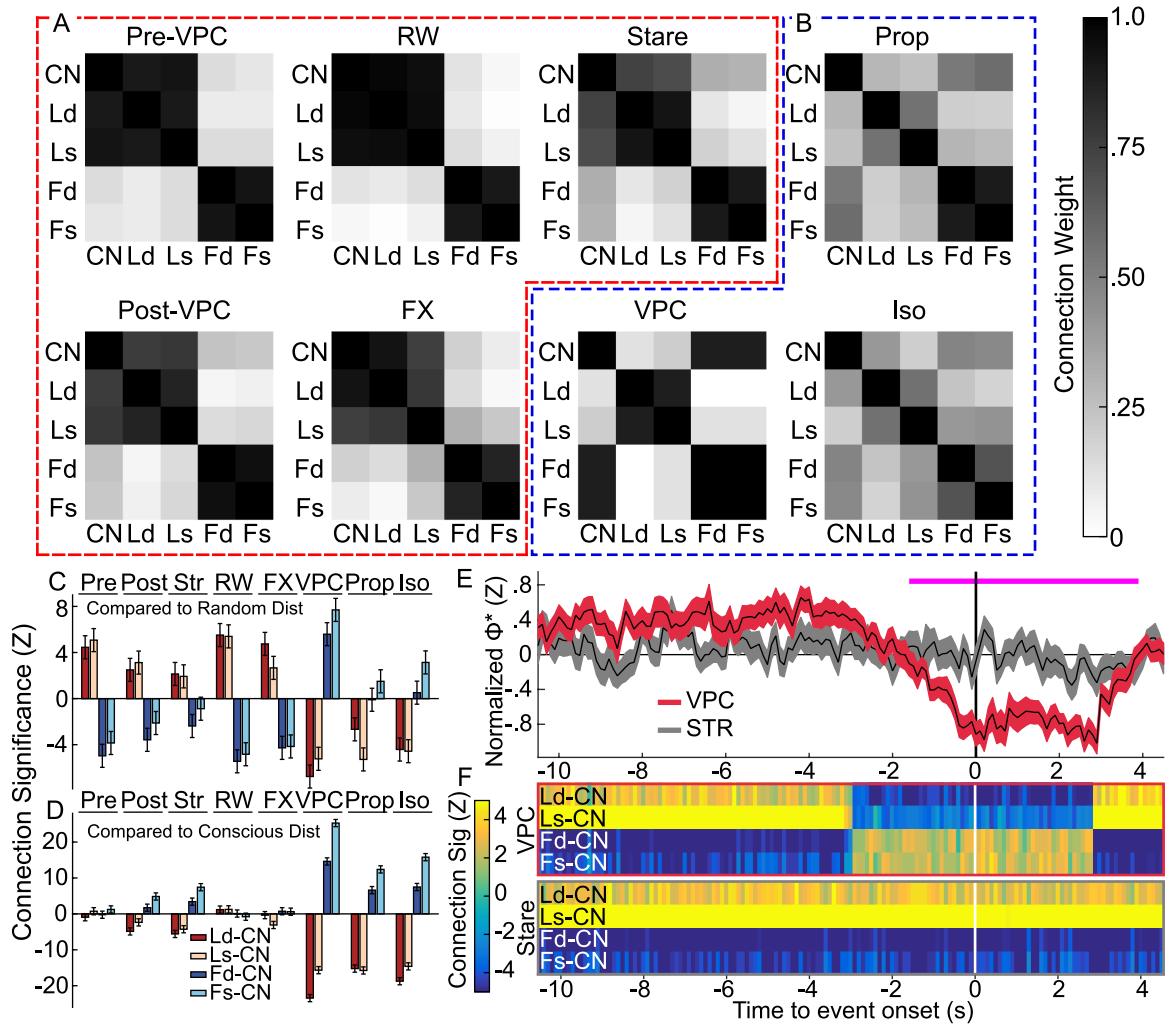
Fig 6. MIP changes reflect switches in parieto-striatal association indicative of consciousness. A, **B**, Probability (connection weight) of each brain area associating with any other on the same side of the MIP for states assumed to be (**A**) conscious (pre-VPC, post-VPC, resting wake (RW), fixation task (FX) and control stares) or (**B**) less conscious (VPC, propofol (Prop), or isoflurane (Iso)). **C, D**, Results (Z statistics ± SD of the null distribution) of the permutation test comparing cortico-striatal MIP associations under the null hypotheses that (**C**) MIP types occur randomly, or (**D**) MIP types reflect the same patterns as conscious states (defined by the resting wake and fixation task samples). Both approaches separate more conscious from less conscious states. **E**, Normalized Φ^* (±SE) for VPC and control stares (STR) calculated in 1s sliding windows (.1s steps) and aligned to event onset (black vertical line). Horizontal pink line shows regions of significance for the pairwise t-test across time comparing VPC Φ^* at each sample to the maximum. No significant differences were found in the control stare condition. **F**, Cortico-striatal significance (Z) based on the sliding window approach in E for VPC and stare conditions. Computations used the same approach as in C, but now for each sample in the sliding window.

https://doi.org/10.1371/journal.pcbi.1010294.g006

conditions, CN commonly associated with parietal regions in pre/post-VPC, STR, resting wakefulness and fixation task (Fig 6A, red dashed border), but associated with frontal regions in VPC, isoflurane and propofol (Fig 6B, blue dashed border). We have previously shown a similar switch in configuration to reflect changes in consciousness [20]. These configuration differences were substantial relative to those expected by chance. Ld-CN connection differences were especially strong and significant ($|Z| \geq 2.15$, $p_c \leq .0312$, Nboot = 10000, permutation test) compared to a null distribution (Fig 6C). To further link this effect to consciousness, we simulated a null distribution representing consciousness by randomly selecting combinations of MIPs found in the wake or fixation task conditions. For VPC, isoflurane and propofol,

the associations of CN with cortical areas Ld, Ls, Fd, and Fs were all substantially different ($|Z| \geq 6.62$, $p \leq 3.62 \times 10^{-11}$, Nboot = 10000, permutation test) relative to the expected distribution under consciousness (Fig 6D). These results imply that network-level activity during VPC events shifts into a configuration associated with a reduction in consciousness.

We computed Φ^* in 1s sliding windows (.1s steps) leading up to, and beyond, the behavioral onset of VPC and control stare events (Fig 6E and 6F). We analyzed data 10.5 seconds prior to event onset, and up to 4.5 seconds after, as these limits represented the maximum consistent duration across all events. On average, Φ^* began to decrease about 3.0s before VPC onset (Fig 6E), when the MIP configuration switched from what is commonly seen in conscious states to the MIP most favored under anesthesia (Fig 6F). This change in MIP configuration continued until 2.9s after VPC onset when it switched back to the wake-favoring MIP. Following the MIP switch, Φ^* was significantly lower than the maximum value between -1.6 and 3.9s relative to event onset ($|t(82)| \geq 3.72$, n = 84, $p_c \leq 0.049$, paired t-tests) for VPC, but was stable during control stares and never significantly lower than the maximum (Fig 6E). Similarly, the MIP configuration during control stares remained in the wake-favoring configuration throughout and never changed relative to event onset (Fig 6F). These results imply that the decreases in consciousness associated with VPC predate the onset of abnormal behavior by 1-3s.

VPC, not control stares, are modulated by thalamic DBS in a frequency-dependent manner across acute and long-term time scales

We argue below that thalamic DBS (specifically at 10 and 200Hz) induces atypical network dynamics biasing towards VPC. That is, not all VPC events occurred as the direct result of an individual DBS stimulation, but rather, VPC in general is modulated by the entire experimental history of DBS in a frequency-dependent manner. We performed 338 experiment blocks in the resting wake condition. VPC events were significantly more common during recording blocks that included thalamic DBS (23.13%, n = 37) than those without (12.92%, n = 23, Z = -2.45, p = .014). Each block involved periods of no stimulation with three replicated stimulation epochs (Fig 2). VPC was significantly more likely to occur within the bounds of the stimulations (64.86%, n = 24) than outside (35.14%, n = 13) compared to a null distribution representing random occurrence (Z = 2.36, p_c = .036, n = 37, permutation test). Moreover, VPC events were overrepresented near the onset (Fig 7A) of a stimulation epoch (within 2s of stimulation onset, 25%, n = 6; Z = -2.58, p = .031, Nboot = 100,000, permutation test). These results imply that thalamic DBS serves as a trigger for VPC under certain conditions.

In line with our hypotheses, VPC probability was higher with 10Hz (23.9%) and 200Hz (30.0%) stimulations, than it was for 50Hz (14.8%) and no-stimulation controls (12.9%) (Fig 7B). Permutation tests revealed that 200Hz stimulations gave rise to significantly increased probability of VPC (Z = 2.71, p_c = .025, Nboot = 100,000, permutation test) compared to the average occurrence (17.8%), while experiments without stimulation (NS) had a significantly decreased probability (Z = -2.44, p_c = .044, Nboot = 100,000, permutation test). We found similar results with causal power (CP, Fig 7D–7F), a probability ratio indicating the strength of causal relationship between two variables relative to alternatives (see METHODS). Positive or negative CP indicates that a given cause (stimulation condition) increases or decreases effect likelihood (VPC occurrence) more so than other known plausible causes [68]. Across the experimental history for both monkeys, CP was typically positive for 200Hz and 10Hz stimulations, and negative for no stimulation and 50Hz stimulation (Fig 7C and 7D). Simulated null-distribution tests indicated causal power for VPC was significantly positive for 200 Hz stimulations (ΔCP = .175, Z = 2.66, p = .031, Nboot = 100,000, permutation test), and significantly
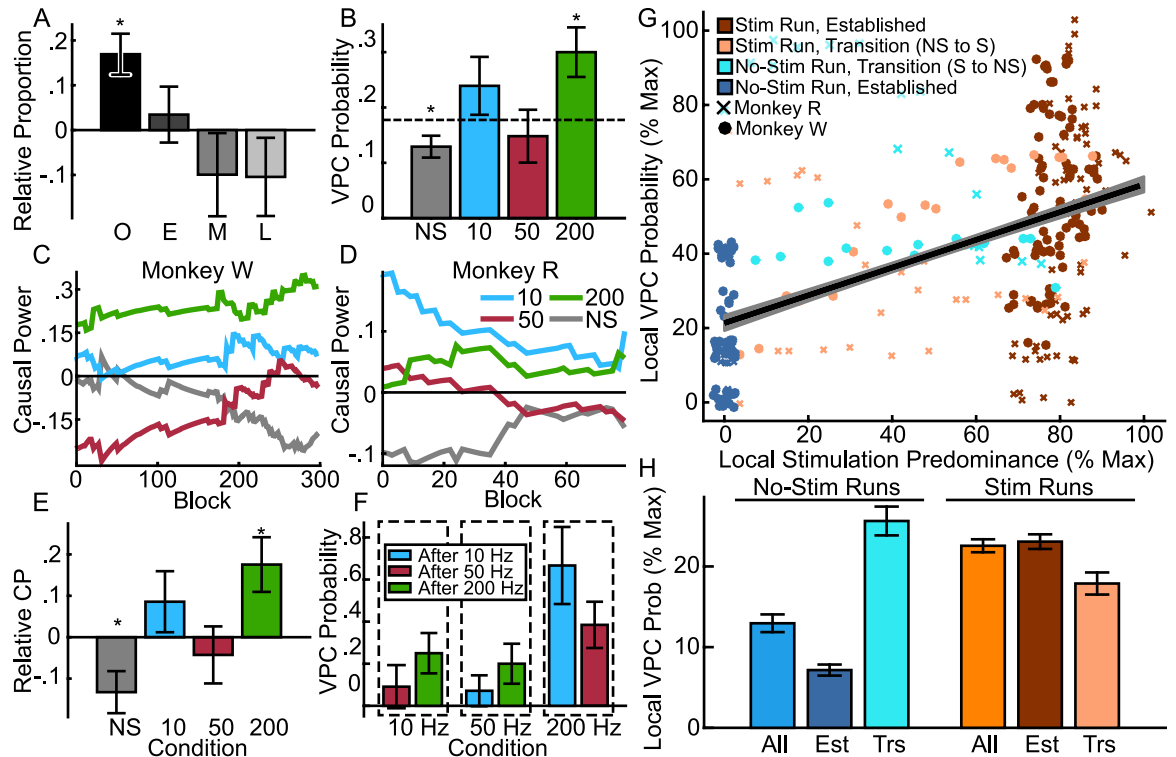
Fig 7. Thalamic DBS modulates VPC occurrence over acute and longer time frames. A, Relative proportion (± SD of the null distribution) of VPC events occurring around the onset (O, within 2 secs of stimulation start), early (E, 2-10s), middle (10-40s), or late (40-60s) phase of the 60s stimulations. **B**, Probability of VPC (± SD of the null distribution) across different experimental conditions: no stimulation (NS) and stimulations at 10, 50 and 200Hz. Dashed line indicates the average probability of VPC (the null hypothesis). **C, D**, Causal power by stimulation condition across experimental history (x axis starting when there are at least 10 blocks per condition to ensure robust causal power estimates) for (**C**) Monkey W and (**D**) Monkey R. **E**, Population CP (± SD of the null distribution) under the null hypothesis that CP is equal across conditions and no different from 0. **F**, Conditional probability (± SD of the null distribution) of VPC occurring with a particular stimulation frequency (10, 50 or 200Hz), given it was preceded by a different stimulation condition, under the null hypothesis that probability of VPC is consistent irrespective of preceding stimulations. **G**, Correlation (best fit line ± SE of the point estimate) of local VPC probability and stimulation predominance (% maximum, sliding window across 32 recording blocks). Individual data points shown for both animals (R and W) across stimulation and no-stimulation runs during transitional (first two days) and established (third day onwards) phases of an experimental series. **H**, Local VPC probability (± SE) for all data (All) in stimulation or no-stimulation runs, and further separated into established (Est) and transitional (Trs) phases.

negative for no stimulation (ΔCP = -.133, Z = -2.58, p = .031, Nboot = 100,000, permutation test) relative to expectations under a null distribution. These results imply that abnormally high frequency activity applied to CL promotes VPC with our DBS method.

The occurrence of VPC also appeared to depend on the stimulation order. In our study, we pseudorandomly assigned the order of stimulation experiments between no-stimulation control, 10Hz, 50Hz and 200Hz conditions (Fig 2) within each experimental run. Thus, for established days in a stimulation series, we could compare the probability of VPC occurring during blocks with a given stimulation frequency relative to that of the preceding stimulation (Fig 7F). Interestingly, 50Hz stimulations, while the least likely to produce VPC, were more likely to do so if preceded by a 200Hz (CP = .091) rather than 10Hz stimulation (CP = -.147). 10Hz stimulations more commonly exhibited VPC after 200Hz (CP = .063) relative to 50Hz (CP = -.273) stimulations; and 200Hz stimulations more commonly exhibited VPC after 10Hz (CP = .515) relative to 50Hz (CP = .038) stimulations. Although none of these effects reached significance with permutation tests (due to the reduced sample sizes when considering all possible combinations of stimulation conditions), the synergistic effect of 10Hz on 200Hz was trending

(Z = 1.63, p = .102, Nboot = 100,000, permutation test). Though the limited power of these analyses does not warrant strong claims, it is still interesting to note that abnormal stimulation frequencies relative to CL (10Hz and 200Hz) both tend to exacerbate VPC and have positive CP. In comparison, 50 Hz stimulations, which we have previously shown to increase consciousness in macaques [4], tend to have negative CP and decrease VPC occurrence.

Irrespective of stimulation frequency, VPC probability increased with the proportion of DBS blocks over consecutive days (Fig 7G). When computing the probability of VPC in sliding windows across 32 blocks (approximating 4 experimental runs and 2 recording days), the local probability of VPC was positively correlated (Fig 7G) with the predominance of stimulations within the same window (r = .5105, t(309) = 10.40, p = 6.54x10^{-16}). Control stares were not significantly correlated with stimulations (r = -.0466, t(309) = -.82, p = .4141). An interaction model verified that the effect of stimulation predominance on event probability was substantially different between VPC and control stares (F(613) = 68.043, n = 618, p = 9.79x10^{-16}, ANCOVA). Our experimental paradigm consisted of shifting between series of recording days that either included stimulation or did not, and each series typically lasted for at least one week, with the first two days of a series being considered transitional (Fig 2). VPC on no-stimulation experimental runs was less common (38.33%, n = 23) than those with stimulation (61.67%, n = 37; Z = -2.45, p = .014, Nboot = 100,000, permutation test). Further, local event probability was significantly higher for experimental runs that included thalamic DBS (Fig 7H, "All" bars) compared to those that did not (t(613) = 6.639, p = 6.96x10^{-11}, n = 618, t-test). This effect was substantially larger than the same effect computed for stare controls, yielding a significant interaction (F(618) = 18.787, n = 618, p = 1.71x10^{-5}, ANCOVA). Interestingly, local VPC probability was higher in the transition period for no-stimulation series, i.e., when the previous few recording days had included thalamic DBS, and decreased markedly after the series was established (Fig 7H). In contrast, local VPC probability was reduced when transitioning from a no-stimulation into a stimulation series, and increased after the series was established. A 3-way ANCOVA verified these effects were significant and specific to VPC events rather than stare controls; the three-way interaction of experimental series type (Stim, No-Stim), establishment (Transition, Established), and event (VPC vs Control Stare) was significant (F(609) = 92.294, n = 618, p = 2.00x10^{-16}, ANCOVA). These results imply that thalamic DBS influences the prevalence of VPC over longer periods of time. Thus, while DBS can directly initiate VPC events, it can also produce longer-duration vulnerabilities that gradually dissipate after stimulation experiments end.

We also included a fixation task in this study as a control (331 experimental blocks recorded), where DBS did not have the same effect. VPC only occurred on 2.72% of fixation task blocks compared to 17.75% of resting wake blocks; this difference was significant (Z = 6.389, p = 1.67x10^{-10}, Nboot = 100,000, permutation test).

VPC events correspond to reduced neural firing

We compared the firing rate of the same neurons, normalized to the pre-condition, across VPC, control stare, post, resting wake and fixation task epochs (although this reduced the relatively small sample size further, it better enabled comparisons with all controls). Firing rates were very similar to the pre-condition for all conditions except VPC (Fig 8). While all areas had lower firing on average during VPC, this difference was only significant for Fs (t(22) = -4.16, n = 23, p_c = .002), Ld (t(32) = -3.06, n = 33, p_c = .022), and CN (t(13) = -3.22, n = 14, p_c = .027). The effect was trending in CL (with a relatively small sample size, as CL recordings only occurred during experiments without thalamic DBS) after multiple comparisons control
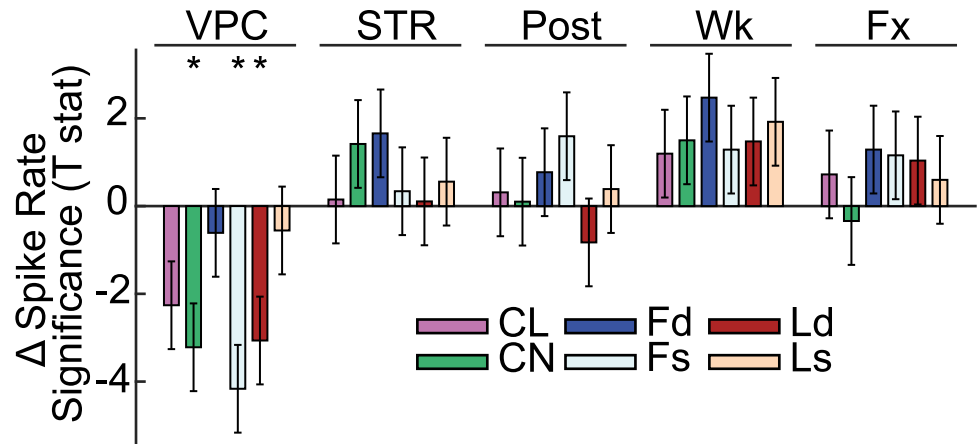
Fig 8. Neural firing rates decrease during VPC relative to control conditions. Spike rate differences normalized to the pre-condition (± SE of the point estimate) for different brain areas under VPC, control stare (STR), post, resting wake (RW), and fixation (FX) conditions. Neurons were analyzed in resting wake, fixation, and pre/post-event epochs only for neurons recorded during VPC or STR events ($N_{CL} = 60$, $N_{CN} = 19$, $N_{Fd} = 15$, $N_{Fs} = 38$, $N_{Ld} = 46$, $N_{Ls} = 21$).

($t(25) = -2.26$, $n = 26$, $p = .033$, $p_c = .098$). These results could reflect changes in neural gain/ excitability, or reduced drive along specific input pathways.

Reduced consciousness in VPC is associated with increases in low-frequency power spectral density

To further evaluate neural signatures of decreased consciousness, we compared LFP spectrograms in different brain regions between all available VPC and control stare conditions relative to event onset. In general, power tended to be lower 3-5s prior to VPC onset (Fig 9A–9F). This was strongest in CL (Fig 9F) which had a significant cluster from θ-γ_H frequencies from approximately -5 to -1.8s relative to event onset (Tsum = -650.76, p = 9.99x10⁻⁵, Nboot = 10,000). Power tended to increase in most areas at low frequencies just prior to event onset, and remain elevated at lower frequencies, especially in Ls (Fig 9B) and Ld (Fig 9D), as the event continued. Power in CL tended to be much higher -1 to 4s around onset, especially at θ and α frequencies. Fig 9F shows the significant cluster (Tsum = 282.74, p = 0.0013, Nboot = 10,000). See Table 1 for full statistical results.

To further investigate the changes in power spectral density influencing VPC, we trained a Bayesian classifier to differentiate between VPC events and control stares, using the LFP power in different frequency bands (δ, θ, α, β, and γ_L) from CN, Ld, Ls, Fd, and Fs calculated in 1s sliding windows (0.5s stride) relative to event onset. CL was excluded because it was only available on a subset of samples, hindering convergence of the parameter estimators. Decoding was significant (Fig 10A) as early as 4s prior to event onset and remained significant thereafter ($|t_{-4 \text{ to } 4.5}(9)| \geq 4.66$, $n = 10$, $p_c \leq .0272$). This window was very similar to the time course of changes in Φ^* (Fig 6E and 6F). We used mean decrease in accuracy (MDA) analysis to estimate which of the LFP features (5 areas x 5 frequency bands) contributed most to decoding accuracy across time (Fig 10B). The MDA is computed by comparing accuracy when the machine learning model includes all possible features to an impoverished model where the information content of a feature has been negated by permuting the sample orders. The greater the MDA, the greater the contribution of that feature. Prior to event onset (-2.5 to -0.5s, Fig 10A, blue horizontal bar), exclusion of CN_β, $Ld_{\theta,\alpha,\beta}$, or $Ls_{\theta,\alpha}$ resulted in the largest decreases in accuracy. Overall, features from Ld (Fig 10C, $|t(1998)| \geq 253$, $n = 2000$, $p_c \leq 1.4x10^{-15}$), and features
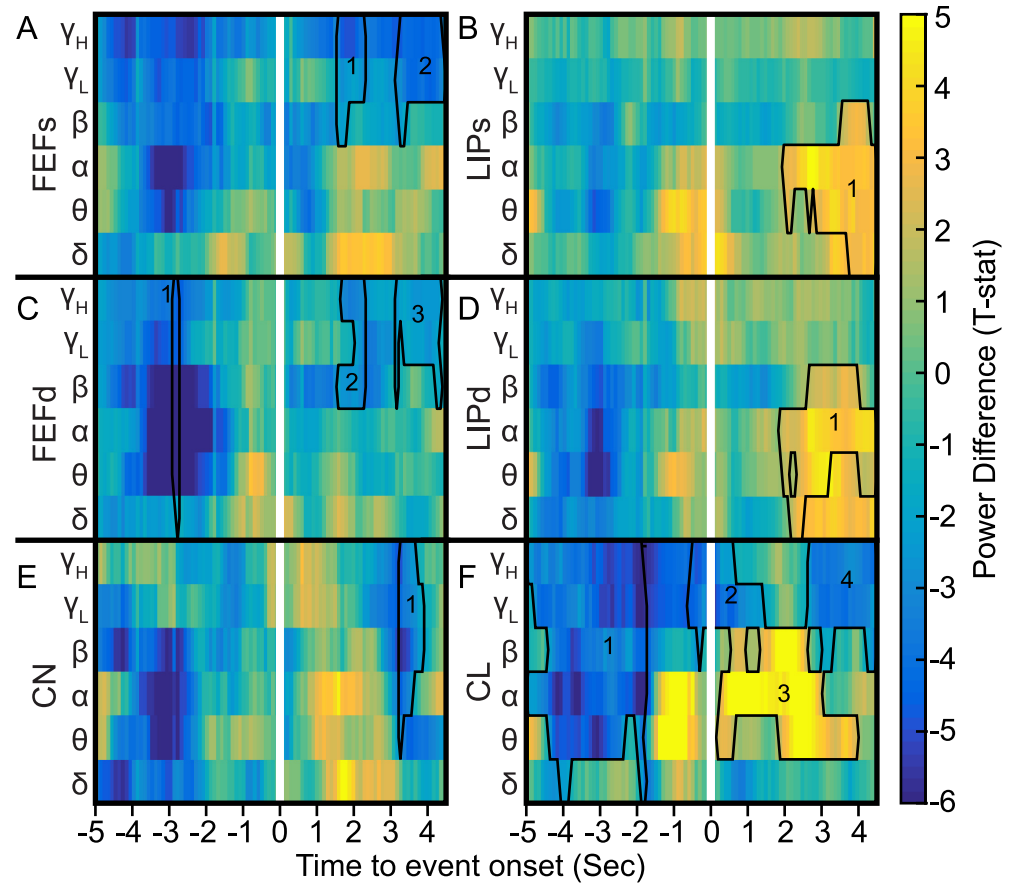
Fig 9. VPC is associated with increases in low-frequency power relative to control stares. A-F Spectrograms of power differences (VPC–control stare) for each frequency band across time aligned to event onset (white vertical line). Results include all recorded VPC and control stares for (**A**) superficial FEF, (**B**) superficial LIP, (**C**) deep FEF, (**D**) deep LIP, (**E**) CN, and (**F**) only the subset of events without thalamic DBS for CL. Significant clusters are outlined in black with numerical labels referenced in Table 1 for statistical details.

related to β power (Fig 10D, $|t(1998)| \geq 253$, n = 2000, $p_c \leq 1.4 \times 10^{-15}$) conveyed more information than others before events.

Between .5 to 4.5s following VPC onset (Fig 10A, thick red horizontal bar), feature importance shifted to lower frequencies. Feature importance was significantly higher for δ, θ, and α frequencies, and lower for β and γ frequencies after the shift ($|t(1998)| \geq 127.3$, n = 2000, $p_c \leq 1.0 \times 10^{-15}$). The importance of CN significantly increased, and importance decreased for all other areas ($|t(1998)| \geq 78.75$, n = 2000, $p_c \leq 1.0 \times 10^{-15}$). Overall, features from CN and Ld (Fig

Table 1. Statistical results of cluster analysis for LFP power spectral density time-frequency spectrograms. Area identity (Tp), N (VPC, control stare), cluster identity, T_{sum} statistic, and p-value for each significant cluster as identified in Fig 9. Positive T_{sum} indicates VPC power spectral density > control stare.

Tp	N	Clust	T_{sum}	p	Tp	N	Clust	T_{sum}	p	Tp	N	Clust	T_{sum}	p
CL	345, 506	1	-650.76	0.0001	FEFd	331,291	1	-61.94	0.0328	FEFs	451, 445	1	-60.18	0.0296
		2	-122.71	0.0347			2	-52.51	0.0494			2	-107.86	0.0035
		3	282.74	0.0013			3	-60.74	0.0343	LIPs	492, 525	1	197.50	0.0077
		4	-143.94	0.0222	LIPd	572, 548	1	183.84	0.0063	CN	1156, 1149	1	-81.64	0.0003
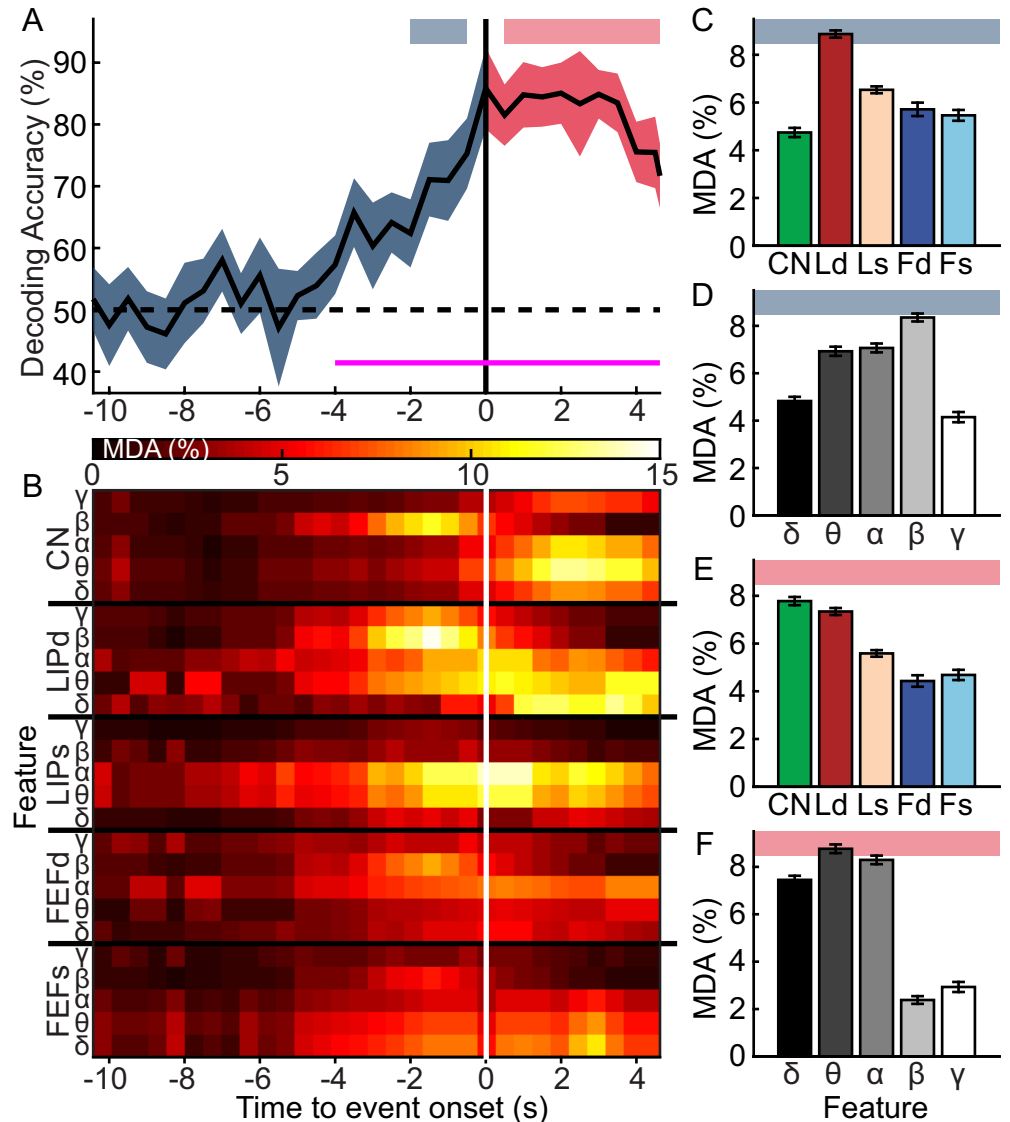
Fig 10. VPC and stare controls are readily decodable on a similar time-frame as changes in consciousness, and represent a clear shift in the relative importance of different frequencies. A, Decoding accuracy (±SE) across time relative to event onset of VPC and stare controls using 25 frequency (δ, θ, α, β, γ) by brain area (CN, Ld, Ls, Fd, Fs) features. Thin saturated pink line shows period of significance when decoding accuracy is greater than chance (50%). **B** Mean decrease in accuracy (MDA) attributed to each model feature across time. Higher values indicate higher feature importance. **D-F**, MDAs further analyzed for the period of time just prior to event onset (thick blue horizontal bar in (**A**)) for features by (**C**) area and (**D**) frequency, and for the period of time just after VPC onset (thick red horizontal bar in (**A**)) for features by (**E**) area and (**F**) frequency. Bar graphs show average MDA (± SD).

10E, $|t(1998)| \geq 210.56$, n = 2000, $p_c \leq 2.0\text{x}10^{-15}$), and features related to δ, θ, and α power (Fig 10F, $|t(1998)| \geq 552.2$, n = 2000, $p_c \leq 1.6\text{x}10^{-15}$) conveyed more information than others (see Fig 10B for the most important individual features, i.e., $CN_{\delta,\theta,\alpha}$, $Ld_{\delta,\theta}$, $Ls_{\theta,\alpha}$, and Fs_{δ}). These results indicate that VPC is associated with a substantial increase in low frequency activity between 1–15 Hz. As this activity is most substantial and informative when found in subcortical and parietal structures, these regions may play the largest role in inducing and promoting VPC.

Reduced consciousness in VPC is associated with changes in CST functional connectivity

To evaluate functional connectivity signatures associated with reduced consciousness, we compared LFP-LFP coherence between the different brain regions representing anatomically-motivated pathways (Fig 11A) relative to event onset between VPC and STR conditions. Changes in coherence were substantial and dynamic across time, leading to a large number of significant clusters (Table 2) in time-frequency coherograms. Thalamo-cortical coherence (Fig 11B and 11C) increased transiently at δ about 3.5s before onset, followed by θ and α about 2.5s before onset (CL-Fs cluster 3, CL-Fd clusters 4 and 5, CL-Ls cluster 2, and, CL-Ld cluster 4, Tsum $\geq$ 43.23, p $\leq$ .0084, Nboot = 10,000). This θ and α coherence only lasted about 1.5s in thalamo-frontal pathways (Fig 11B), but continued in thalamo-parietal pathways (Fig 11C) at least 1.5s after event onset, matching the time course of abnormal θ dynamics exhibited by CL.

About 3-4s before onset, cortico-striatal coherence (Fig 11D) in θ and α bands decreased along the frontal projection (Fd-CN cluster 1, Tsum = -187.32, p = 0.0001, Nboot = 10,000) and increased along the parietal projection (Ld-CN cluster 1, Tsum = 865.22, p = 0.0001, Nboot = 10,000). Fronto-striatal increases started about a second later, and both fronto- and parieto-striatal coherence persisted, especially at δ, throughout the VPC event (Fd-CN cluster 4 and 8, Ld-CN cluster 2, Tsum $\geq$ 49.95, p $\leq$ 0.0167, Nboot = 10,000).

Just before VPC onset, CL became internally coherent (Fig 11E) at θ frequencies relative to control stares. This effect lasted from approximately -2.5 to 3.5 s relative to onset (CL-CL cluster 5, Tsum = 837.28, p = 0.001, Nboot = 10,000), matching the time course associated with decreases in Φ^*. Thalamo-striatal coherence (Fig 11E) increased at low frequencies (θ, α) just before VPC onset (CL-CN cluster 4, Tsum = 269.84, p = 0.0001, Nboot = 10,000) relative to control stares and remained elevated only briefly thereafter (CL-CN cluster 7, Tsum = 167.29, p = 0.0001, Nboot = 10,000). Striato-striatal coherence (Fig 11E), in comparison, exhibited a transient, broadband increase right at VPC onset (CN-CN cluster 4, Tsum = 491.94, p = 0.0001, Nboot = 10,000).

Intracolumnar coherence (Fig 11F) was initially increased at higher frequencies (β, γ_L, and γ_H) (Fs-Fd cluster 2, Ls-Ld cluster 2, Tsum $\geq$ 333.07, p $\leq$ 0.0001, Nboot = 10,000). Coherence then shifted to lower frequencies (δ, θ, and α) just before event onset and continued after VPC onset (Fs-Fd cluster 3, Ls-Ld cluster 3, Tsum $\geq$ 299.02, p $\leq$ 0.0001, Nboot = 10,000). These effects appeared to be more consistent in parietal regions relative to frontal. We have previously demonstrated similar shifts in intracolumnar coherence to lower frequencies during general anesthesia [4]. This could imply that VPC is associated with perturbation of intracolumnar signaling, thereby contributing to sensory disconnection and reductions in consciousness.

Cortico-cortical interactions involve feedforward (FF) pathways, carrying sensory information from superficial layers of parietal cortex to superficial or middle layers of frontal cortex. Feedback (FB) pathways carry predictions and priorities from the deep layers of frontal cortex to the superficial or deep layers of parietal regions [76,77]. Around 3s before VPC onset, FF and FB coherence (Fig 11G) showed broadband increases (Ls-Fs clusters 2–4, Fd-Ls cluster 3, Fd-Ld cluster 2, Tsum $\geq$ 72.11 p $\leq$ 0.0039, Nboot = 10,000) that dissipated just before event onset (-3 to -1 s). At onset, there were transient broadband decreases in putative Fd-Ls feedback (Fd-Ls cluster 4, Tsum = -133.75, p = 0.0002, Nboot = 10,000), but more persistently, a decrease in putative feedforward Ls-Fs coherence that extended to about 2.5s after onset (Ls-Fs cluster 5, Tsum = -291.08, p = 0.0001, Nboot = 10,000). This latter effect could imply a form of sensory disconnect.
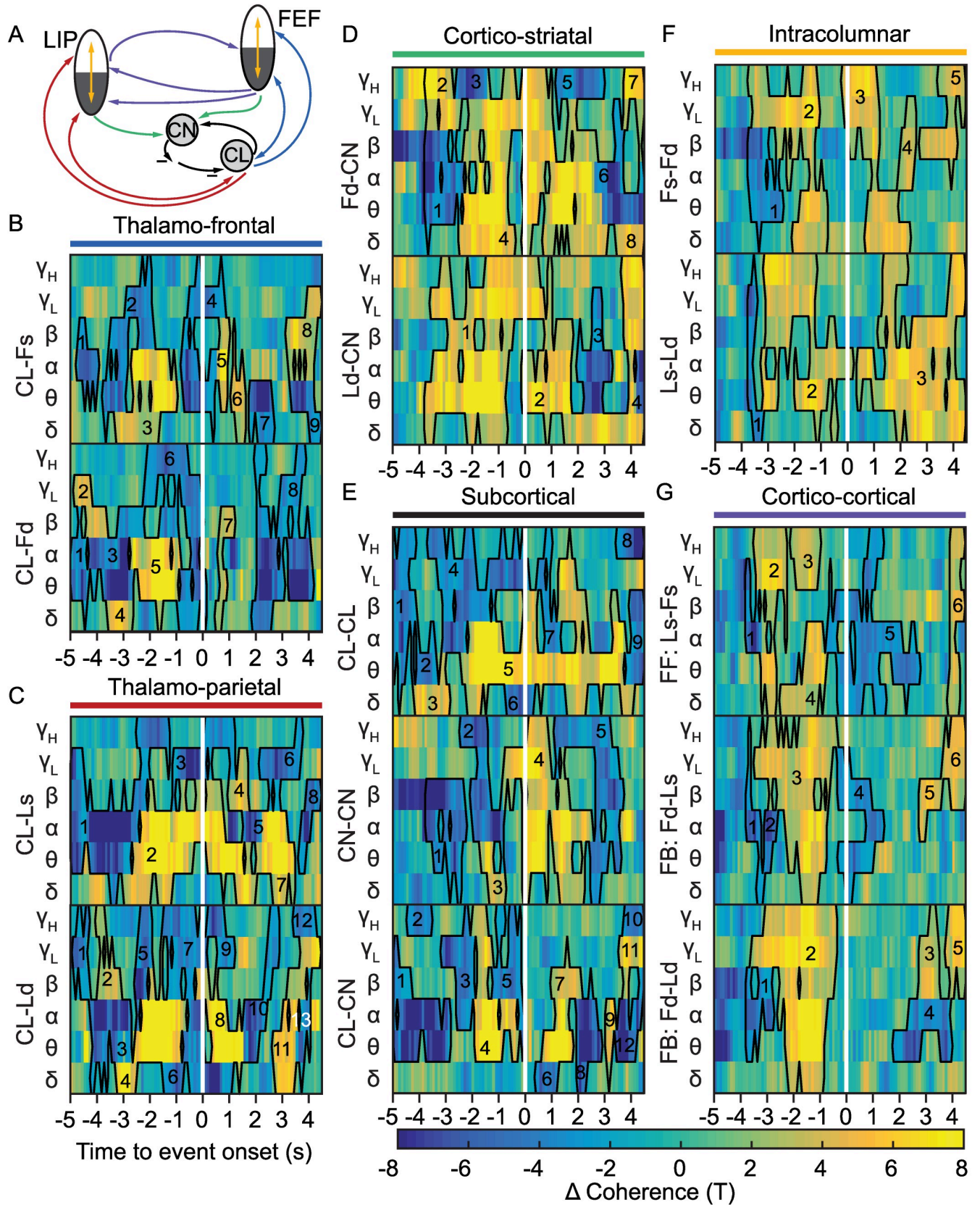
Fig 11. Functional connectivity increases, especially at low frequencies, just before and throughout VPC. A, Diagram showing anatomical pathways isolated in our study. Superficial and deep cortical layers are represented by the respective light and dark regions of the labeled area. Arrow colors relate to the panel subtitle underlines featured in B-G. **B-G**, Time-frequency plots showing coherence differences (VPC–control stare) aligned to event onset (white vertical line) for pairs of LFPs within/between brain area(s). Color scales with the strength of the resulting t-stat. Significant clusters are outlined in black with numerical labels referenced in Table 2 for statistical details. Results are shown for the key (**B**) Thalamo-frontal, (**C**) Thalamo-parietal, (**D**) Cortico-striatal, (**E**) Subcortical, (**F**) Intracolumnar, and (**G**) Cortico-cortical feedforward (FF, Ls-Fs) and feedback (FB, Fd-Ld and Fd-Ls) pathways.

To summarize the complex temporal dynamics across all relevant pathways, we compared the percentage of significant time-frequency tiles (hereon referred to as pixels) within different temporal windows, indicating increases or decreases in high (β,γ_L,γ_H) or low (δ,θ,α) frequency coherence (Fig 12). This can be considered the predominance of different coherence patterns. Window P1 (Fig 12A, -5 to -2.6s) represents the period of time prior to event onset where decoding accuracy (based on power spectral density) is low and differences in consciousness (Φ^*) are insignificant. Significant pixels are rare in this period, indicating similarities in coherence between VPC and control events. Most significant pixels that are present reflect decreases in low-frequency coherence between CL and other regions. Window P2 (Fig 12B, -2.5 to -0.6s) represents the time period prior to event onset where decoding accuracy increases, and decreases in Φ^* become significant. This corresponds to an increase in the number of significant pixels indicating increases in low-frequency coherence. These changes span most pathways, but especially those involving CN and deep layers of cortical areas, where the effects are more broadband. At the same time, pixels representing the relationship between CL and other areas reflect high-frequency decreases in coherence, whereas cortico-cortical pathways have increased coherence at higher frequencies predominating.

Window EO (Fig 12C, -.5 to .5s) represents the second of data around event onset, where decoding has reached maximum accuracy and changes in Φ^* hit the minimum Φ^* value. In this window, the majority of pixels representing the relationship between cortex and CN reflect broadband coherence increases. At the same time, there are broadband decreases in coherence predominating for pathways connecting CL to other areas. Window A1 (Fig 12D, .6 to 2.5s) represents the first two seconds after event onset, where decoding remains high and decreases in Φ^* remain significant. In this window, there is increased low-frequency coherence within areas (Fig 12D, third row, along diagonal), but not between most areas. Finally, in window A2 (Fig 12E, 2.5 to 4.5s) when behavioral signs of VPC are still present, significant decoding persists and Φ^* is gradually returning towards the baseline level, there is predominantly increased low-frequency coherence in parietal cortex, in addition to CL.

Discussion

We used thalamic DBS to induce acute and spontaneous perturbations in consciousness (VPC events). These events include long-duration, vacant stares coinciding with lower-frequency EEG activity and decreases in neural measures of complexity and integration indicative of consciousness. VPC was best predicted by power changes in parietal cortex and striatum relative to frontal cortex. Just before VPC events, consciousness, as indexed by Φ^*, decreased as lower-frequency coherence increased between cortical and subcortical regions (Fig 13A). There was a burst of broadband coherence between the cortex and striatum around VPC onset (Fig 13B), which was followed by dominant lower-frequency coherence within each cortical and subcortical area during VPC (Fig 13C), indicative of increased isolation of individual areas. VPC also involved reduced firing rate in superficial FEF, which could result from reduced input, reflected in the decreased broadband coherence of the feedforward pathway during VPC.

We also saw reduced firing rates in LIP deep layers during VPC reminiscent of the reduced excitability of deep-layer cortical neurons previously shown under anesthesia [4,13], which

Table 2. Statistical results of cluster analysis for coherence time-frequency spectrograms. Area identity (Tp), N (VPC, control stare), cluster identity (Clust), T_{sum} statistic, and p-value for each significant cluster as identified in Fig 11. Positive T_{sum} indicates VPC coherence > control stare.

Tp	N	Clust	T_{sum}	p	Tp	N	Clust	T_{sum}	p	Tp	N	Clust	T	p	Tp	N	Clust	T	p
Fs-Fd	2771, 2323	1	-116.87	.0011	CL-CN	3465, 4637	1	-333.13	0.0001	CL-CL	3782, 5780	1	-131.95	.0001	CL-Ld	3979, 5750	1	-54.84	0.0021
		2	333.07	.0001			2	-36.22	0.0260			2	-40.44	.0227			2	-188.44	0.0001
		3	299.02	.0001			3	-118.78	0.0001			3	66.20	.0007			3	46.27	0.0058
		4	49.06	.0457			4	269.84	0.0001			4	-308.18	.0001			4	488.59	0.0001
		5	115.36	.0011			5	-96.93	0.0001			5	837.28	.0001			5	-84.19	0.0002
CN-CN	9210, 7429	1	-214.37	.0001			6	-38.46	0.0194			6	-55.89	.0028			6	-270.48	0.0001
		2	-180.25	.0001			7	167.29	0.0001			7	-50.69	.0069			7	-32.86	0.0403
		3	47.02	.0238			8	-167.55	0.0001			8	-64.49	.0011			8	199.91	0.0001
		4	491.94	.0001			9	32.06	0.0480			9	-77.52	.0003			9	-55.44	0.0019
		5	-236.95	.0001			10	-33.17	0.0410	CL-Fd	2346, 3611	1	-54.68	0.0024			10	-114.06	0.0001
CL-Fs	1671, 2805	1	-64.36	.0008			11	56.90	0.0017			2	58.93	0.0017			11	175.65	0.0001
		2	-152.52	.0001			12	-129.83	0.0001			3	-221.02	0.0001			12	-32.70	0.0410
		3	232.90	.0001	Fd-CN	7225, 6051	1	-187.32	0.0001			4	43.23	0.0084			13	-36.16	0.0244
		4	-174.43	.0001			2	120.42	0.0002			5	234.34	0.0001	FB: Fd-Ls	3024, 2730	1	-49.66	0.0173
		5	54.39	.0023			3	-65.03	0.0046			6	-246.83	0.0001			2	-42.19	0.0364
		6	45.71	.0069			4	1172.33	0.0001			7	41.06	0.0121			3	425.92	0.0001
		7	-101.51	.0001			5	-79.73	0.0013			8	-416.88	0.0001			4	-133.75	0.0002
		8	84.27	.0001			6	-184.60	0.0001	CL-Ls	2790, 4472	1	-506.52	0.0001			5	50.35	0.0165
		9	-67.26	.0006			7	65.75	0.0044			2	694.73	0.0001			6	91	0.0008
Ld-CN	11844, 11212	1	865.22	.0001			8	49.95	0.0167			3	-123.74	0.0001	FF: Ls-Fs	3444, 2881	1	-52.99	0.0128
		2	527.41	.0001	FB: Fd-Ld	4098, 3733	1	-83.93	0.0034			4	42.64	0.0084			2	181.11	0.0001
		3	-148.01	.0001			2	713.05	0.0001			5	-40.22	0.01220			3	72.11	0.0039
		4	-44.37	.0151			3	62.89	0.0102			6	-89.60	0.0001			4	122.02	0.0002
Ls-Ld	5172, 4774	1	-64.13	.0038			4	-135	0.0002			7	208.93	0.0001			5	-291.08	0.0001
		2	392.41	.0001			5	91.18	0.0022			8	-56.74	0.0014			6	93.21	0.0011
		3	648.07	.0001																

* Nboot = 10,000
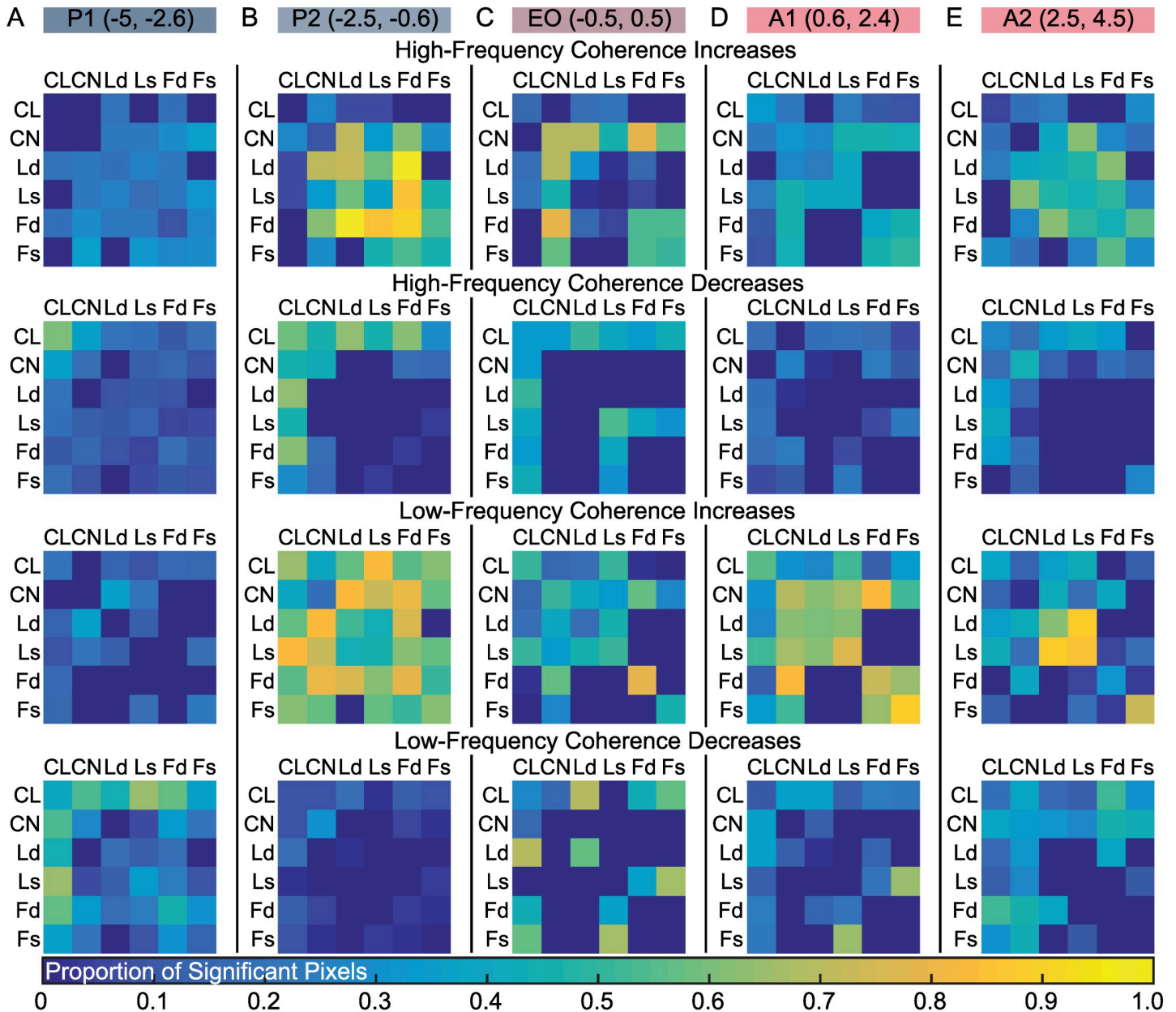
Fig 12. Pathways involving thalamus and striatum dominate the changes in coherence attributed to VPC. A-E, For each pairwise comparison across all areas, proportion of significant pixels indicating coherence increases/decreases at higher-frequency (β, γ_L, γ_H) or increases/decreases at lower-frequency (δ, θ, α) in time windows that (**A**) predate significant decoding and changes in consciousness (Pre 1, P1), (**B**) coincide with increased decoding and the start of changes in consciousness (Pre 2, P2), (**C**) coincide with behavioral changes (event onset, EO), (**D**) coincide with sustained changes in behavior and consciousness (After 1, A1), and (**E**) coincide with changed behavior but gradual restoration of consciousness as gauged with Φ^* (After 2, A2).

could result from perturbed intracolumnar communication. Overall, these patterns reflect disruption of typical CST network dynamics, resulting in reduced behavior and consciousness.

The nature of VPC

The VPC state that we describe in this manuscript proved inconsistent with many naturalistic states observed in macaques. Despite EEG signatures of reduced consciousness and reductions
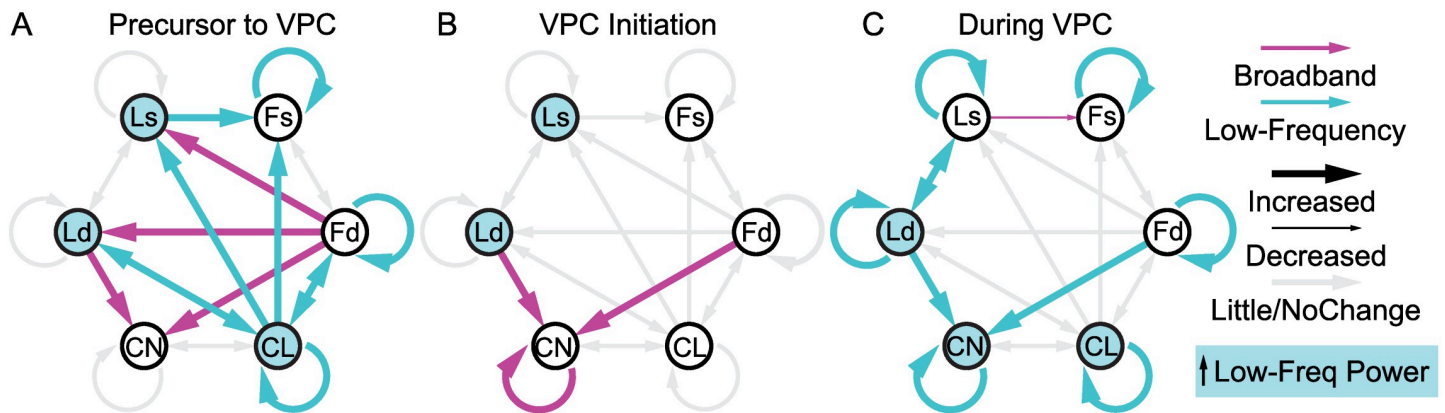
Fig 13. Neural correlates of VPC involve substantial impairment of communication in thalamo-cortical and cortico-striatal circuits. A-C, Connection diagrams summarizing key coherence and power patterns within and between different areas (**A**) just before, (**B**) at onset, and (**C**) ongoing during VPC. Arrows show increased (thicker) or decreased (thinner) coherence between specified areas at lower (light blue) or broadband (pink) frequencies. Light gray arrows indicate pathways where coherence changes are relatively small or unchanged. Blue shading in areas shows power increases at low frequencies. Ls and Ld, superficial and deep layers of LIP; Fs and Fd, superficial and deep layers of FEF; CN, caudate nucleus; CL, central lateral thalamus. Diagrams summarize results from Figs 9–11, and values thresholded at .4 in Fig 12.

https://doi.org/10.1371/journal.pcbi.1010294.g013

in integration and complexity, VPC was not associated with drowsiness or general decreases in arousal. Animals remained upright with their eyes wide open. VPC was also behaviorally inconsistent with goal-directed attention, despite stillness and decreased eye movement. During vacant stares the eye position would typically freeze and then drift at a very slow rate, unlike either visual search or the goal-oriented fixations observed during task performance.

During rest, it is possible to engage in internally-directed activity such as mind-wandering, typically associated with reduced attention to the external environment [78] and shifts in functional network connectivity towards default mode dynamics [79]. Reduced external attention may explain the vacant staring observed during VPC. However, internally-directed states are not expected to involve substantial reductions in the brain's overall capacity for carrying information nor the complexity of information flow [80], but rather a different allocation of neural resources [78]. We found that VPC involved significant reductions in both H and Φ^*, reflecting reduced complexity of neural dynamics and information-carrying capacity. Such reductions in H and Φ^* were not observed when comparing on-task behavior (fixation task) relative to resting wakefulness, despite the conditions being distinguished by different levels of attention and the sensory experience of reward. But reductions in H and Φ^* were observed in the same recorded network and animals during sleep or general anesthesia [20]. Thus, even if VPC does not involve observable decreases in arousal, it does appear to involve neural processes more typical of a loss of consciousness.

If VPC does not resemble typical wakeful states, perhaps it better resembles abnormal conditions induced by chemical intervention or disease. For example, VPC could be similar to dissociative states induced by psychedelics, which do often alter activity in cortico-striato-thalamic networks [21,81] in some ways similar to VPC. However, behavioral changes during psychedelic use [82] are typically different to those observed during VPC. Further, prevailing evidence and theories about the effect of psychedelics suggest that they will cause increases in measures of complexity, such as entropy [83–85]. Rather, an intriguing possibility is that VPC is related to epileptic disorders, such as temporal lobe or absence epilepsy [30,43,73]. Generally speaking, these conditions are associated with a loss of consciousness despite sustained behavioral arousal with reduced but repetitive motor movements, i.e., automatisms. For absence

epilepsy, seizures coincide with reduced neural complexity [86], just like VPC. Further, absence epilepsy, which in humans is associated with the sudden onset of vacant staring during an episode, is a particularly close match to the behavioral signature of VPC [43–45]. Moreover, just as VPC appeared to be initiated and kindled by thalamic DBS, similar to mechanisms known to influence seizure rates in epilepsies [87], so too has thalamic DBS triggered absence epilepsy in a number of past studies [26,88,89].

Shared mechanisms connect VPC to absence epilepsy

Intralaminar thalamic DBS was originally reported to induce decreases in consciousness such as sleep or behavioral arrest in cats [88]. VPC matches the description of the arrest reaction as described by Hunter and Jasper (1949), which included sudden decreases in behavior with reduced responsiveness to sensory stimuli. The arrest reaction sometimes progressed into a state resembling an absence seizure [88], complete with 3 Hz spike-and-wave oscillations common to absence epilepsy [43–45]. Subsequent thalamic DBS studies have been able to replicate these effects in both cats [26] and monkeys [89]. Similar in effect, our study used a unique thalamic DBS protocol to produce VPC, which shares many behavioral correlates with absence epilepsy, including the sudden onset of vacant staring and the small mouth and eye movements consistent with automatisms [43–45]. Further, our results reveal considerable overlap between the neural mechanisms of VPC and absence. Absence epilepsy has long been associated with altered thalamocortical activity [90], including substantial increases in thalamocortical coherence [91]. Our VPC events were triggered by thalamic DBS, and initiated with increased low-frequency coherence along thalamocortical pathways, especially involving parietal cortex. More recently, evidence has also pointed to the importance of cortico-striatal [23,24,46,92] dynamics in absence seizures and, in rodent models, dopaminergic manipulation in the striatum can even modulate seizures [93]. Similarly, we found lower-frequency coherence changes along cortico-striatal pathways, and ongoing decreases in striatal firing rate were also characteristic of VPC.

The chief distinction between VPC and absence epilepsy is the presence of 3Hz spike-wave patterns in the EEG during absences. We observed increased oscillatory activity during VPC in the absence range (3-8Hz), though it lacked the characteristic spike-and-wave patterns attributed to the disorder in humans [43–45] and animal models [43–46]. One possibility for this discrepancy is that, while VPC seems to share mechanisms with absence, which can be triggered by thalamic DBS [88,89,94], it represents a pre-epileptic version of the syndrome that does not include spike-and-wave pathology. Previous work in cats implies that progression from behavioral arrest to 3Hz spike-and-wave absence events is possible [88] but difficult to replicate and may require stimulation of the thalamic reticular nucleus [26]. Our stimulation protocol involved a multi-microelectrode approach with relatively low-current (200µA) stimulations, which were based on parameters we have previously used to manipulate consciousness under anesthesia [4]. As other studies have shown, higher-current stimulations may be more likely to progress effects like VPC to epileptic activity [88]. In monkeys, absence responses with thalamic DBS are more common in drowsy animals [89] and after premotor cortical lesions [94,95], while our animals were intact, and recordings took place during the typical wakeful period. All of these results imply that VPC may be a sub-epileptic condition, useful for studies of consciousness. A further implication is that intralaminar thalamic DBS would more specifically model absence epilepsy if stimulation parameters were tailored to that effect, for example, using bilateral stimulations at higher current.

The mechanistic links between VPC and absence epilepsy are informative for clinical populations. Foremost, the similarity in symptoms between VPC and absence seizures, even

without spike-and-wave patterns, could imply that these 3Hz rhythms are correlated with, but not necessarily causal towards, loss of consciousness during absences. In line with this, while rodent genetic models of absence epilepsy show spike-and-wave pathology [46], spike-and-wave discharges have also been reported in wild-type rodents [96]. In humans, absence seizures can present with abnormal or disorganized spike-wave morphology [97], and their overall clarity and severity can vary both within and between patients [43]. Additionally, the frequency of spike-and-wave oscillations can be variable over the course of a seizure, typically starting faster and slowing over time [89,98,99]. Further, oscillations in animals are typically higher in frequency than those reported in humans, ranging up to 6Hz in macaques [89,100], or from 5-10Hz in rodents [46]. Thus, while spike-and-wave pathology is likely important for absence epilepsy, it may not be directly causal towards mechanisms of loss of consciousness. Rather, they may result as a consequence of the same abnormal thalamocortical dynamics which seem to trigger VPC in this study, and absence events in clinical populations [43]. If so, loss of consciousness is likely more closely linked to perturbed functional connectivity in CST networks.

Mechanisms of multi-microelectrode DBS

This study used multi-microelectrode DBS to manipulate consciousness in a frequency-dependent manner. Instead of larger DBS electrodes commonly used clinically, our stimulating electrodes were linear microelectrode arrays designed to conform to CL dimensions in macaques (Fig 1). Previously, we used this DBS method to increase consciousness in anesthetized macaques in a frequency-dependent manner that was CL-selective and maximally effective at 50Hz [4]. This result contrasts with another recent study achieving similar arousing effects using more traditional methodology, but at a much higher stimulation frequency (150Hz) and current (1.0–2.0mA vs our 200μA) [5]. These discrepancies could imply a fundamental difference in mechanism between the DBS methods. It is possible that the multi-microelectrode method more directly influences the targeted nucleus in ways that match the stimulation parameters.

This interpretation is supported by our current study, where thalamic DBS modulated VPC at both acute and longer-duration time scales. VPC was most strongly driven by 200Hz or 10Hz perturbations, both of which represent abnormal dynamics for CL in wakefulness, relative to 50Hz stimulation, which produced modulatory effects no stronger than no-stimulation controls. Further, VPC was most common when 200Hz stimulations followed 10Hz blocks. 10Hz activity is more similar to the dynamics of CL during sleep [4,29], while 200Hz represents, over longer time scales, non-physiological activity, or possibly the short inter-spike intervals within bursts generated by many other thalamic neurons in reduced conscious states. In comparison, 50Hz matches the dynamics of fast-firing CL neurons during wakefulness [4,28,29]. Clinically, absence seizures are associated with reduced arousal and are more common after sleep deprivation [101], and thalamic DBS more readily triggers absence-like responses in drowsy [89] or lightly anesthetized animals [102]. Similarly for VPC, 10Hz stimulations might reduce arousal and increase low-frequency oscillatory activity which propagates throughout the CST network. As our results show, such oscillations within CST areas predominate during VPC (Fig 12C). In addition, low-frequency coherence in the CST network often predates the onset of VPC (Fig 12A and 12B). Subsequent 200Hz stimulations, which might either mimic thalamic bursting or even lead to a shutdown of CL, capitalize on this vulnerability and thus induce VPC more often than other conditions. The fact that our results are frequency-specific, and these frequencies are functionally relevant for CL, implies that our method exerts effects by mimicking outputs of CL, and not through antidromic mechanisms.

Optimizing paradigms to produce VPC

VPC was associated with stimulation onset, implying that DBS directly influences CST dynamics to promote VPC. Further, VPC became more prevalent as stimulations were performed more frequently, even occurring without DBS application. These results imply that vulnerability to CST circuit disruptions linger and contribute to future disruptions in consciousness, not dissimilar to kindling effects in seizure models [87]. Our stimulations lasted for one minute, and were replicated three times per stimulation block, with multiple blocks performed each day. This paradigm could induce neural plasticity [103,104] promoting abnormal network dynamics that both exacerbate future responses to DBS and increase the likelihood for resting-state dynamics to spontaneously give way to VPC events. Similar mechanisms seem to contribute to epilepsy, as seizures commonly alter functional connectivity over the course of the disease, with the effect size dependent on seizure rate [105]. Interestingly for VPC, plasticity seemed to depend on exposure to the stimulation paradigm, as after experiments ceased, no abnormal events have been observed by experimenters or care staff during everyday behavior.

These results suggest that experimental parameters could be optimized to increase the rate of VPC beyond those we observed. Others have employed bilateral stimulation [3,106], which may produce stronger effects than our unilateral approach. Further, our experiments incorporated factors which decreased VPC likelihood (fixation task, no-stimulation blocks, 50Hz stimulations). Their inclusion in this study serve as controls that help link VPC to related states of decreased consciousness. For example, studies have shown that seizure rates tend to decrease with cognitive engagement in animal models [107], and VPC is similarly rare during fixation tasks. However, including the fixation task, no-stimulation blocks and 50Hz stimulations likely limited the overall occurrence of VPC well below what is possible with our stimulation method. Our results imply that the stimulation effects could increase with repeated batteries of 10Hz and 200Hz stimulations, which trended towards a synergistic effect. Such optimizations increasing VPC likelihood could further enable perceptual experiments in which sensory stimuli are presented during VPC or without perturbing consciousness. Increasing the VPC rate from DBS is likely to also increase the spontaneous VPC rate during non-stimulation transitions, which would further reduce potential confounds, such as artifacts caused by DBS.

VPC and neural correlates of consciousness in CST networks

This study builds on recent findings about CST circuitry during different conscious states. We previously showed that Φ^*, a measure of neural integration, differentiates wakefulness, sleep, and anesthesia [20]. Here, Φ^* further differentiates resting wakefulness, fixation tasks and stare controls from VPC. The time course of changes in Φ^* map onto the time course of our ability to decode VPC from control stare events based on cortical and subcortical LFP power, as well as dynamic changes in CST network coherence. In this study, atypical broadband increases in coherence between cortex and striatum were linked to decreased consciousness at VPC onset, just as ongoing low-frequency intra-area coherence was linked to reduced consciousness during VPC events. Critically, this implies that different patterns of aberrant activity can contribute to reduced Φ^* and consciousness in CST circuits.

Decreased consciousness also temporally aligned with changes in the integrated structure of the CST network (Fig 6), such that frontal regions, rather than parietal, became more affiliated with subcortical structures. This finding during VPC generalizes network configuration changes for reduced consciousness under two separate anesthetic agents and, as previously shown, during non-rapid-eye-movement sleep [20]. These findings challenge cortico-centric assumptions about consciousness. Affiliation of parietal and subcortical structures during wakefulness may represent parieto-striatal-thalamic interactions promoting sensory

processing and perceptual representations. Shifts of subcortical affiliations to frontal cortex could represent breakdowns in the aforesaid more posterior associative networks and sensory pathways, resulting in decreases in consciousness.

The question remains how disruption of thalamic activity with DBS spreads across the CST network to perturb consciousness. The thalamus could disrupt cortico-striatal interactions by either directly influencing cortex, and consequently cortico-striatal projections, or via thalamo-striatal projections that directly modulate striatal responses [108]. Our results suggest the former has a greater influence. Thalamic DBS caused interference in thalamic outputs which translated to cortico-striatal, more so than thalamo-striatal, perturbations (Figs 11, 12 and 13). Abnormal cortico-striatal inputs likely alter basal ganglia output to the thalamus, further perturbing thalamo-cortical, cortico-cortical and cortico-striatal processes. Overall, our results highlight the influential role of the basal ganglia and higher-order thalamic structures, which control information processing and flow through CST networks in ways that support and manipulate consciousness [18,109]. This challenges common assumptions about the relevance of subcortical brain areas in consciousness research [17,110] which is of great importance to clinical practice.

Acknowledgments

Author Contributions

Conceptualization: Michelle J. Redinbaugh, Yuri B. Saalmann.

Data curation: Michelle J. Redinbaugh, Mohsen Afrasiabi.

Formal analysis: Michelle J. Redinbaugh, Mohsen Afrasiabi, Yuri B. Saalmann.

Funding acquisition: Yuri B. Saalmann.

Investigation: Michelle J. Redinbaugh, Jessica M. Phillips, Niranjan A. Kambi, Sounak Mohanta, Aeyal Raz, Yuri B. Saalmann.

Project administration: Yuri B. Saalmann.

Writing – original draft: Michelle J. Redinbaugh, Mohsen Afrasiabi, Yuri B. Saalmann.

Writing – review & editing: Michelle J. Redinbaugh, Mohsen Afrasiabi, Jessica M. Phillips, Niranjan A. Kambi, Sounak Mohanta, Aeyal Raz, Yuri B. Saalmann.

References

1. Chiken S, Nambu A. Mechanism of Deep Brain Stimulation: Inhibition, Excitation, or Disruption? Neuroscientist. 2016; 22(3):313–22. Epub 2015/04/19. https://doi.org/10.1177/1073858415581986 PMID: 25888630; PubMed Central PMCID: PMC4871171.

2. Perlmutter JS, Mink JW. Deep brain stimulation. Annu Rev Neurosci. 2006; 29:229–57. Epub 2006/06/17. https://doi.org/10.1146/annurev.neuro.29.051605.112824 PMID: 16776585; PubMed Central PMCID: PMC4518728.

3. Schiff ND, Giacino JT, Kalmar K, Victor JD, Baker K, Gerber M, et al. Behavioural improvements with thalamic stimulation after severe traumatic brain injury. Nature. 2007; 448(7153):600–3. https://doi.org/10.1038/nature06041 PMID: 17671503.

4. Redinbaugh MJ, Phillips JM, Kambi NA, Mohanta S, Andryk S, Dooley GL, et al. Thalamus Modulates Consciousness via Layer-Specific Control of Cortex. Neuron. 2020; 106(1):66–75. Epub 2020/02/14. https://doi.org/10.1016/j.neuron.2020.01.005 PMID: 32053769.

5. Bastos AM, Donoghue JA, Brincat SL, Mahnke M, Yanar J, Correa J, et al. Neural effects of propofol-induced unconsciousness and its reversal using thalamic stimulation. Elife. 2021;10. Epub 2021/04/28. https://doi.org/10.7554/eLife.60824 PMID: 33904411; PubMed Central PMCID: PMC8079153.

6. Oizumi M, Albantakis L, Tononi G. From the phenomenology to the mechanisms of consciousness: Integrated Information Theory 3.0. PLoS Comput Biol. 2014; 10(5):e1003588. https://doi.org/10.1371/journal.pcbi.1003588 PMID: 24811198; PubMed Central PMCID: PMC4014402.

7. Dehaene S, Changeux JP. Experimental and theoretical approaches to conscious processing. Neuron. 2011; 70(2):200–27. Epub 2011/04/28. https://doi.org/10.1016/j.neuron.2011.03.018 PMID: 21521609.

8. Friston K. The free-energy principle: a unified brain theory? Nat Rev Neurosci. 2010; 11(2):127–38. Epub 2010/01/14. https://doi.org/10.1038/nrn2787 PMID: 20068583.

9. Lamme VA. Towards a true neural stance on consciousness. Trends Cogn Sci. 2006; 10(11):494–501. Epub 2006/09/26. https://doi.org/10.1016/j.tics.2006.09.001 PMID: 16997611.

10. Kaufman EF, Rosenquist AC. Efferent projections of the thalamic intralaminar nuclei in the cat. Brain Res. 1985; 335(2):257–79. Epub 1985/06/03. https://doi.org/10.1016/0006-8993(85)90478-0 PMID: 4005555.

11. Towns LC, Tigges J, Tigges M. Termination of thalamic intralaminar nuclei afferents in visual cortex of squirrel monkey. Vis Neurosci. 1990; 5(2):151–4. Epub 1990/08/01. https://doi.org/10.1017/s0952523800000195 PMID: 2278942.

12. Senzai Y, Fernandez-Ruiz A, Buzsaki G. Layer-Specific Physiological Features and Interlaminar Interactions in the Primary Visual Cortex of the Mouse. Neuron. 2019; 101(3):500–13 e5. Epub 2019/01/13. https://doi.org/10.1016/j.neuron.2018.12.009 PMID: 30635232; PubMed Central PMCID: PMC6367010.

13. Suzuki M, Larkum ME. General Anesthesia Decouples Cortical Pyramidal Neurons. Cell. 2020; 180 (4):666–76 e13. Epub 2020/02/23. https://doi.org/10.1016/j.cell.2020.01.024 PMID: 32084339.

14. Smith Y, Galvan A, Ellender TJ, Doig N, Villalba RM, Huerta-Ocampo I, et al. The thalamostriatal system in normal and diseased states. Front Syst Neurosci. 2014; 8:5. Epub 2014/02/14. https://doi.org/10.3389/fnsys.2014.00005 PMID: 24523677; PubMed Central PMCID: PMC3906602.

15. Smith Y, Raju DV, Pare JF, Sidibe M. The thalamostriatal system: a highly specific network of the basal ganglia circuitry. Trends Neurosci. 2004; 27(9):520–7. Epub 2004/08/28. https://doi.org/10.1016/j.tins.2004.07.004 PMID: 15331233.

16. Jones EG. The thalamus. 2nd ed. Cambridge; New York: Cambridge University Press; 2007.

17. Boly M, Massimini M, Tsuchiya N, Postle BR, Koch C, Tononi G. Are the Neural Correlates of Consciousness in the Front or in the Back of the Cerebral Cortex? Clinical and Neuroimaging Evidence. J Neurosci. 2017; 37(40):9603–13. Epub 2017/10/06. https://doi.org/10.1523/JNEUROSCI.3218-16.2017 PMID: 28978697; PubMed Central PMCID: PMC5628406.

18. Schiff ND. Recovery of consciousness after brain injury: a mesocircuit hypothesis. Trends Neurosci. 2010; 33(1):1–9. https://doi.org/10.1016/j.tins.2009.11.002 PMID: 19954851; PubMed Central PMCID: PMC2931585.

19. Tononi G. An information integration theory of consciousness. BMC Neurosci. 2004; 5:42. https://doi.org/10.1186/1471-2202-5-42 PMID: 15522121; PubMed Central PMCID: PMC543470.

20. Afrasiabi M, Redinbaugh MJ, Phillips JM, Kambi NA, Mohanta S, Raz A, et al. Consciousness depends on integration between parietal cortex, striatum, and thalamus. Cell Syst. 2021; 12(4):363–73 e11. Epub 2021/03/18. https://doi.org/10.1016/j.cels.2021.02.003 PMID: 33730543; PubMed Central PMCID: PMC8084606.

21. Preller KH, Razi A, Zeidman P, Stampfli P, Friston KJ, Vollenweider FX. Effective connectivity changes in LSD-induced altered states of consciousness in humans. Proc Natl Acad Sci U S A. 2019; 116 (7):2743–8. Epub 2019/01/30. https://doi.org/10.1073/pnas.1815129116 PMID: 30692255; PubMed Central PMCID: PMC6377471.

22. Mhuircheartaigh RN, Rosenorn-Lanng D, Wise R, Jbabdi S, Rogers R, Tracey I. Cortical and subcortical connectivity changes during decreasing levels of consciousness in humans: a functional magnetic resonance imaging study using propofol. J Neurosci. 2010; 30(27):9095–102. https://doi.org/10.1523/JNEUROSCI.5516-09.2010 PMID: 20610743.

23. Berman R, Negishi M, Vestal M, Spann M, Chung MH, Bai X, et al. Simultaneous EEG, fMRI, and behavior in typical childhood absence seizures. Epilepsia. 2010; 51(10):2011–22. Epub 2010/07/09. https://doi.org/10.1111/j.1528-1167.2010.02652.x PMID: 20608963; PubMed Central PMCID: PMC2953613.

24. Carney PW, Masterton RA, Harvey AS, Scheffer IE, Berkovic SF, Jackson GD. The core network in absence epilepsy. Differences in cortical and thalamic BOLD response. Neurology. 2010; 75(10):904–11. Epub 2010/08/13. https://doi.org/10.1212/WNL.0b013e3181f11c06 PMID: 20702791.

25. Schiff ND. Central thalamic contributions to arousal regulation and neurological disorders of consciousness. Ann N Y Acad Sci. 2008; 1129:105–18. https://doi.org/10.1196/annals.1417.029 PMID: 18591473.

26. Ingvar DH. Reproduction of the 3 per second spike and wave EEG pattern by subcortical electrical stimulation in cats. Acta Physiol Scand. 1955; 33(2–3):137–50. Epub 1955/01/01. https://doi.org/10.1111/j.1748-1716.1955.tb01200.x PMID: 14387760.

27. Liu J, Lee HJ, Weitz AJ, Fang Z, Lin P, Choy M, et al. Frequency-selective control of cortical and subcortical networks by central thalamus. Elife. 2015; 4:e09215. Epub 2015/12/15. https://doi.org/10.7554/eLife.09215 PMID: 26652162; PubMed Central PMCID: PMC4721962.

28. Glenn LL, Steriade M. Discharge rate and excitability of cortically projecting intralaminar thalamic neurons during waking and sleep states. J Neurosci. 1982; 2(10):1387–404. Epub 1982/10/01. https://doi.org/10.1523/JNEUROSCI.02-10-01387.1982 PMID: 7119864.

29. Steriade M, Curro Dossi R, Contreras D. Electrophysiological properties of intralaminar thalamocortical cells discharging rhythmic (approximately 40 HZ) spike-bursts at approximately 1000 HZ during waking and rapid eye movement sleep. Neuroscience. 1993; 56(1):1–9. Epub 1993/09/01. https://doi.org/10.1016/0306-4522(93)90556-u PMID: 8232908.

30. Blumenfeld H. Impaired consciousness in epilepsy. Lancet Neurol. 2012; 11(9):814–26. Epub 2012/08/18. https://doi.org/10.1016/S1474-4422(12)70188-6 PMID: 22898735; PubMed Central PMCID: PMC3732214.

31. Saleem KS, Logothetis NK. A combined MRI and histology atlas of the rhesus monkey brain in stereotaxic coordinates. London; Burlington, MA: Academic; 2007. ix, 326 pages p.

32. Bruce CJ, Goldberg ME, Bushnell MC, Stanton GB. Primate frontal eye fields. II. Physiological and anatomical correlates of electrically evoked eye movements. J Neurophysiol. 1985; 54(3):714–34. Epub 1985/09/01. https://doi.org/10.1152/jn.1985.54.3.714 PMID: 4045546

33. Pettersen KH, Devor A, Ulbert I, Dale AM, Einevoll GT. Current-source density estimation based on inversion of electrostatic forward solution: effects of finite extent of neuronal activity and conductivity discontinuities. J Neurosci Methods. 2006; 154(1–2):116–33. Epub 2006/01/27. https://doi.org/10.1016/j.jneumeth.2005.12.005 PMID: 16436298.

34. Caruso VC, Pages DS, Sommer MA, Groh JM. Similar prevalence and magnitude of auditory-evoked and visually evoked activity in the frontal eye fields: implications for multisensory motor control. J Neurophysiol. 2016; 115(6):3162–73. Epub 2016/03/05. https://doi.org/10.1152/jn.00935.2015 PMID: 26936983; PubMed Central PMCID: PMC4946597.

35. Romanski LM, Tian B, Fritz J, Mishkin M, Goldman-Rakic PS, Rauschecker JP. Dual streams of auditory afferents target multiple domains in the primate prefrontal cortex. Nat Neurosci. 1999; 2 (12):1131–6. Epub 1999/11/26. https://doi.org/10.1038/16056 PMID: 10570492; PubMed Central PMCID: PMC2778291.

36. Schall JD, Morel A, King DJ, Bullier J. Topography of visual cortex connections with frontal eye field in macaque: convergence and segregation of processing streams. J Neurosci. 1995; 15(6):4464–87. Epub 1995/06/01. https://doi.org/10.1523/JNEUROSCI.15-06-04464.1995 PMID: 7540675

37. Cohen YE, Russ BE, Gifford GW, 3rd. Auditory processing in the posterior parietal cortex. Behav Cogn Neurosci Rev. 2005; 4(3):218–31. Epub 2006/03/03. https://doi.org/10.1177/1534582305285861 PMID: 16510894.

38. Gifford GW 3rd, Cohen YE. Spatial and non-spatial auditory processing in the lateral intraparietal area. Exp Brain Res. 2005; 162(4):509–12. Epub 2005/05/03. https://doi.org/10.1007/s00221-005-2220-2 PMID: 15864568.

39. Brown RE, Basheer R, McKenna JT, Strecker RE, McCarley RW. Control of sleep and wakefulness. Physiol Rev. 2012; 92(3):1087–187. Epub 2012/07/20. https://doi.org/10.1152/physrev.00032.2011 PMID: 22811426; PubMed Central PMCID: PMC3621793.

40. Nir Y, Staba RJ, Andrillon T, Vyazovskiy VV, Cirelli C, Fried I, et al. Regional slow waves and spindles in human sleep. Neuron. 2011; 70(1):153–69. https://doi.org/10.1016/j.neuron.2011.02.043 PMID: 21482364; PubMed Central PMCID: PMC3108825.

41. Purdon PL, Sampson A, Pavone KJ, Brown EN. Clinical Electroencephalography for Anesthesiologists: Part I: Background and Basic Signatures. Anesthesiology. 2015; 123(4):937–60. https://doi.org/10.1097/ALN.0000000000000841 PMID: 26275092; PubMed Central PMCID: PMC4573341.

42. Alkire MT, Hudetz AG, Tononi G. Consciousness and anesthesia. Science. 2008; 322(5903):876–80. https://doi.org/10.1126/science.1149213 PMID: 18988836; PubMed Central PMCID: PMC2743249.

43. Blumenfeld H. Consciousness and epilepsy: why are patients with absence seizures absent? Prog Brain Res. 2005; 150:271–86. Epub 2005/09/28. https://doi.org/10.1016/S0079-6123(05)50020-7 PMID: 16186030; PubMed Central PMCID: PMC3153469.

44. Tenney JR, Glauser TA. The current state of absence epilepsy: can we have your attention? Epilepsy Curr. 2013; 13(3):135–40. Epub 2013/07/11. https://doi.org/10.5698/1535-7511-13.3.135 PMID: 23840175; PubMed Central PMCID: PMC3697883.

45. Hughes JR. Absence seizures: a review of recent reports with new concepts. Epilepsy Behav. 2009; 15(4):404–12. Epub 2009/07/28. https://doi.org/10.1016/j.yebeh.2009.06.007 PMID: 19632158.

46. Coenen AM, Van Luijtelaar EL. Genetic animal models for absence epilepsy: a review of the WAG/Rij strain of rats. Behav Genet. 2003; 33(6):635–55. Epub 2003/10/24. https://doi.org/10.1023/a:1026179013847 PMID: 14574120.

47. Mayanagi Y, Watanabe E, Kaneko Y. Mesial temporal lobe epilepsy: clinical features and seizure mechanism. Epilepsia. 1996; 37 Suppl 3:57–60. Epub 1996/01/01. https://doi.org/10.1111/j.1528-1157.1996.tb01823.x PMID: 8681916

48. Blumenfeld H, McNally KA, Vanderhill SD, Paige AL, Chung R, Davis K, et al. Positive and negative network correlations in temporal lobe epilepsy. Cereb Cortex. 2004; 14(8):892–902. Epub 2004/04/16. https://doi.org/10.1093/cercor/bhh048 PMID: 15084494.

49. Englot DJ, Yang L, Hamid H, Danielson N, Bai X, Marfeo A, et al. Impaired consciousness in temporal lobe seizures: role of cortical slow activity. Brain. 2010; 133(Pt 12):3764–77. https://doi.org/10.1093/brain/awq316 PMID: 21081551; PubMed Central PMCID: PMC2995886.

50. Brown EN, Lydic R, Schiff ND. General anesthesia, sleep, and coma. N Engl J Med. 2010; 363 (27):2638–50. https://doi.org/10.1056/NEJMra0808281 PMID: 21190458; PubMed Central PMCID: PMC3162622.

51. Giacino JT, Fins JJ, Laureys S, Schiff ND. Disorders of consciousness after acquired brain injury: the state of the science. Nat Rev Neurol. 2014; 10(2):99–114. Epub 2014/01/29. https://doi.org/10.1038/nrneurol.2013.279 PMID: 24468878.

52. Bollimunta A, Chen Y, Schroeder CE, Ding M. Neuronal mechanisms of cortical alpha oscillations in awake-behaving macaques. J Neurosci. 2008; 28(40):9976–88. Epub 2008/10/03. https://doi.org/10.1523/JNEUROSCI.2699-08.2008 PMID: 18829955; PubMed Central PMCID: PMC2692971.

53. Haegens S, Barczak A, Musacchia G, Lipton ML, Mehta AD, Lakatos P, et al. Laminar Profile and Physiology of the alpha Rhythm in Primary Visual, Auditory, and Somatosensory Regions of Neocortex. J Neurosci. 2015; 35(42):14341–52. Epub 2015/10/23. https://doi.org/10.1523/JNEUROSCI.0600-15.2015 PMID: 26490871; PubMed Central PMCID: PMC4683691.

54. Trongnetrpunya A, Nandi B, Kang D, Kocsis B, Schroeder CE, Ding M. Assessing Granger Causality in Electrophysiological Data: Removing the Adverse Effects of Common Signals via Bipolar Derivations. Front Syst Neurosci. 2015; 9:189. Epub 2016/02/03. https://doi.org/10.3389/fnsys.2015.00189 PMID: 26834583; PubMed Central PMCID: PMC4718991.

55. Oizumi M, Amari S, Yanagawa T, Fujii N, Tsuchiya N. Measuring Integrated Information from the Decoding Perspective. PLoS Comput Biol. 2016; 12(1):e1004654. Epub 2016/01/23. https://doi.org/10.1371/journal.pcbi.1004654 PMID: 26796119; PubMed Central PMCID: PMC4721632.

56. Barrett AB, Seth AK. Practical measures of integrated information for time-series data. PLoS Comput Biol. 2011; 7(1):e1001052. Epub 2011/02/02. https://doi.org/10.1371/journal.pcbi.1001052 PMID: 21283779; PubMed Central PMCID: PMC3024259.

57. Haun AM, Oizumi M, Kovach CK, Kawasaki H, Oya H, Howard MA, et al. Conscious Perception as Integrated Information Patterns in Human Electrocorticography. eNeuro. 2017; 4(5). Epub 2017/11/01. https://doi.org/10.1523/ENEURO.0085-17.2017 PMID: 29085895; PubMed Central PMCID: PMC5659238.

58. Mediano PA, Seth AK, Barrett AB. Measuring Integrated Information: Comparison of Candidate Measures in Theory and Simulation. Entropy. 2019; 21(1):17. https://doi.org/10.3390/e21010017 PMID: 33266733

59. Henze N, Zirkler B. A class of invariant consistent tests for multivariate normality. Communications in Statistics—Theory and Methods. 1990; 19(10):3595–617. https://doi.org/10.1080/03610929008830400

60. Balduzzi D, Tononi G. Integrated information in discrete dynamical systems: motivation and theoretical framework. PLoS Comput Biol. 2008; 4(6):e1000091. https://doi.org/10.1371/journal.pcbi.1000091 PMID: 18551165; PubMed Central PMCID: PMC2386970.

61. Oizumi M, Tsuchiya N, Amari SI. Unified framework for information integration based on information geometry. Proc Natl Acad Sci U S A. 2016; 113(51):14817–22. Epub 2016/12/09. https://doi.org/10.1073/pnas.1603583113 PMID: 27930289; PubMed Central PMCID: PMC5187746.

62. Toker D, Sommer FT. Information integration in large brain networks. PLoS Comput Biol. 2019; 15(2): e1006807. Epub 2019/02/08. https://doi.org/10.1371/journal.pcbi.1006807 PMID: 30730907; PubMed Central PMCID: PMC6382174.

63. Strong SP, Koberle R, de Ruyter van Steveninck RR, Bialek W. Entropy and Information in Neural Spike Trains. Physical Review Letters. 1998; 80(1):197–200. https://doi.org/10.1103/PhysRevLett.80. 197

64. Brenner N, Strong SP, Koberle R, Bialek W, de Ruyter van Steveninck RR. Synergy in a neural code. Neural Comput. 2000; 12(7):1531–52. https://doi.org/10.1162/089976600300015259 PMID: 10935917.

65. Bishop CM. Pattern recognition and machine learning. New York: Springer; 2006. xx, 738 p. p.

66. Murphy KP. Machine learning: a probabilistic perspective. Cambridge, MA: MIT Press; 2012. xxix, 1067 p. p.

67. Molnar C. Interpretable machine learning. A Guide for Making Black Box Models Explainable 2019.

68. Griffiths TL, Tenenbaum JB. Structure and strength in causal induction. Cogn Psychol. 2005; 51 (4):334–84. Epub 2005/09/20. https://doi.org/10.1016/j.cogpsych.2005.05.004 PMID: 16168981.

69. Salvatier J, Wiecki TV, Fonnesbeck C. Probabilistic programming in Python using PyMC3. PeerJ Computer Science. 2016; 2:e55. https://doi.org/10.7717/peerj-cs.55

70. Gerber EM. permutest. https://www.mathworks.com/matlabcentral/fileexchange/71737-permutest: MATLAB Central File Exchange; 2021.

71. Maris E, Oostenveld R. Nonparametric statistical testing of EEG- and MEG-data. Journal of Neuroscience Methods. 2007; 164(1):177–90. https://doi.org/10.1016/j.jneumeth.2007.03.024 PMID: 17517438

72. Blair RD. Temporal lobe epilepsy semiology. Epilepsy Res Treat. 2012; 2012:751510. Epub 2012/09/ 08. https://doi.org/10.1155/2012/751510 PMID: 22957241; PubMed Central PMCID: PMC3420439.

73. Blumenfeld H, Taylor J. Why do seizures cause loss of consciousness? Neuroscientist. 2003; 9 (5):301–10. Epub 2003/10/29. https://doi.org/10.1177/1073858403255624 PMID: 14580115.

74. Arsiwalla XD, Verschure P. Measuring the Complexity of Consciousness. Front Neurosci. 2018; 12:424. Epub 2018/07/13. https://doi.org/10.3389/fnins.2018.00424 PMID: 29997472; PubMed Central PMCID: PMC6030381.

75. Seth AK, Dienes Z, Cleeremans A, Overgaard M, Pessoa L. Measuring consciousness: relating behavioural and neurophysiological approaches. Trends Cogn Sci. 2008; 12(8):314–21. Epub 2008/07/09. https://doi.org/10.1016/j.tics.2008.04.008 PMID: 18606562; PubMed Central PMCID: PMC2767381.

76. Markov NT, Vezoli J, Chameau P, Falchier A, Quilodran R, Huissoud C, et al. Anatomy of hierarchy: feedforward and feedback pathways in macaque visual cortex. J Comp Neurol. 2014; 522(1):225–59. Epub 2013/08/29. https://doi.org/10.1002/cne.23458 PMID: 23983048; PubMed Central PMCID: PMC4255240.

77. Mejias JF, Murray JD, Kennedy H, Wang XJ. Feedforward and feedback frequency-dependent interactions in a large-scale laminar network of the primate cortex. Sci Adv. 2016; 2(11):e1601335. Epub 2017/02/01. https://doi.org/10.1126/sciadv.1601335 PMID: 28138530; PubMed Central PMCID: PMC5262462.

78. Kam JW, Handy TC. The neurocognitive consequences of the wandering mind: a mechanistic account of sensory-motor decoupling. Front Psychol. 2013; 4:725. Epub 20131014. https://doi.org/10.3389/ fpsyg.2013.00725 PMID: 24133472; PubMed Central PMCID: PMC3796327.

79. Zhou X, Lei X. Wandering Minds with Wandering Brain Networks. Neurosci Bull. 2018; 34(6):1017–28. Epub 20180822. https://doi.org/10.1007/s12264-018-0278-7 PMID: 30136075; PubMed Central PMCID: PMC6246840.

80. Ibanez-Molina AJ, Iglesias-Parro S. Neurocomputational Model of EEG Complexity during Mind Wandering. Front Comput Neurosci. 2016; 10:20. Epub 20160304. https://doi.org/10.3389/fncom.2016. 00020 PMID: 26973505; PubMed Central PMCID: PMC4777878.

81. Riga MS, Llado-Pelfort L, Artigas F, Celada P. The serotonin hallucinogen 5-MeO-DMT alters cortico-thalamic activity in freely moving mice: Regionally-selective involvement of 5-HT1A and 5-HT2A receptors. Neuropharmacology. 2018; 142:219–30. Epub 20171206. https://doi.org/10.1016/j. neuropharm.2017.11.049 PMID: 29221792.

82. Frederick DL, Gillam MP, Lensing S, Paule MG. Acute effects of LSD on rhesus monkey operant test battery performance. Pharmacol Biochem Behav. 1997; 57(4):633–41. https://doi.org/10.1016/s0091-3057(96)00469-8 PMID: 9258988.

83. Carhart-Harris RL. The entropic brain—revisited. Neuropharmacology. 2018; 142:167–78. Epub 20180314. https://doi.org/10.1016/j.neuropharm.2018.03.010 PMID: 29548884.

84. Luppi AI, Carhart-Harris RL, Roseman L, Pappas I, Menon DK, Stamatakis EA. LSD alters dynamic integration and segregation in the human brain. Neuroimage. 2021; 227:117653. Epub 20201215. https://doi.org/10.1016/j.neuroimage.2020.117653 PMID: 33338615; PubMed Central PMCID: PMC7896102.

85. Gallimore AR. Restructuring consciousness -the psychedelic state in light of integrated information theory. Front Hum Neurosci. 2015; 9:346. Epub 20150612. https://doi.org/10.3389/fnhum.2015.00346 PMID: 26124719; PubMed Central PMCID: PMC4464176.

86. Li J, Yan J, Liu X, Ouyang G. Using Permutation Entropy to Measure the Changes in EEG Signals During Absence Seizures. Entropy. 2014; 16(6):3049–61. https://doi.org/10.3390/e16063049

87. Morimoto K, Fahnestock M, Racine RJ. Kindling and status epilepticus models of epilepsy: rewiring the brain. Prog Neurobiol. 2004; 73(1):1–60. Epub 2004/06/15. https://doi.org/10.1016/j.pneurobio.2004.03.009 PMID: 15193778.

88. Hunter J, Jasper HH. Effects of thalamic stimulation in unanaesthetised animals; the arrest reaction and petit mal-like seizures, activation patterns and generalized convulsions. Electroencephalogr Clin Neurophysiol. 1949; 1(3):305–24. Epub 1949/08/01. https://doi.org/10.1016/0013-4694(49)90043-7 PMID: 18135423.

89. Steriade M. Interneuronal epileptic discharges related to spike-and-wave cortical seizures in behaving monkeys. Electroencephalogr Clin Neurophysiol. 1974; 37(3):247–63. Epub 1974/09/01. https://doi.org/10.1016/0013-4694(74)90028-5 PMID: 4136833

90. Matricardi S, Verrotti A, Chiarelli F, Cerminara C, Curatolo P. Current advances in childhood absence epilepsy. Pediatr Neurol. 2014; 50(3):205–12. Epub 2014/02/18. https://doi.org/10.1016/j.pediatrneurol.2013.10.009 PMID: 24530152.

91. Sitnikova E, van Luijtelaar G. Cortical and thalamic coherence during spike–wave seizures in WAG/Rij rats. Epilepsy Research. 2006; 71(2):159–80. https://doi.org/10.1016/j.eplepsyres.2006.06.008 PMID: 16879948

92. Miyamoto H, Tatsukawa T, Shimohata A, Yamagata T, Suzuki T, Amano K, et al. Impaired cortico-striatal excitatory transmission triggers epilepsy. Nat Commun. 2019; 10(1):1917. Epub 2019/04/25. https://doi.org/10.1038/s41467-019-09954-9 PMID: 31015467; PubMed Central PMCID: PMC6478892.

93. Deransart C, Riban V, Le B, Marescaux C, Depaulis A. Dopamine in the striatum modulates seizures in a genetic model of absence epilepsy in the rat. Neuroscience. 2000; 100(2):335–44. Epub 2000/09/29. https://doi.org/10.1016/s0306-4522(00)00266-9 PMID: 11008171.

94. David J, Marathe SB, Patil SD, Grewal RS. Arrest reaction with concomitant spike and wave after-discharge following thalamic stimulation in conscious juvenile monkeys with Al (OH)3 focal premotor lesions. Indian J Physiol Pharmacol. 1981; 25(3):209–18. Epub 1981/07/01. PMID: 7298145.

95. David J, Marathe SB, Patil SD, Grewal RS. Behavioral and electrical correlates of absence seizures induced by thalamic stimulation in juvenile rhesus monkeys with frontal aluminum hydroxide implants: a pharmacologic evaluation. J Pharmacol Methods. 1982; 7(3):219–29. Epub 1982/05/01. https://doi.org/10.1016/0160-5402(82)90038-9 PMID: 6810026.

96. Taylor JA, Reuter JD, Kubiak RA, Mufford TT, Booth CJ, Dudek FE, et al. Spontaneous Recurrent Absence Seizure-like Events in Wild-Caught Rats. J Neurosci. 2019; 39(24):4829–41. Epub 2019/04/12. https://doi.org/10.1523/JNEUROSCI.1167-18.2019 PMID: 30971439; PubMed Central PMCID: PMC6561690.

97. Sadleir LG, Farrell K, Smith S, Connolly MB, Scheffer IE. Electroclinical features of absence seizures in childhood absence epilepsy. Neurology. 2006; 67(3):413–8. Epub 2006/08/09. https://doi.org/10.1212/01.wnl.0000228257.60184.82 PMID: 16894100.

98. Bosnyakova D, Gabova A, Kuznetsova G, Obukhov Y, Midzyanovskaya I, Salonin D, et al. Time-frequency analysis of spike-wave discharges using a modified wavelet transform. J Neurosci Methods. 2006; 154(1–2):80–8. Epub 2006/01/26. https://doi.org/10.1016/j.jneumeth.2005.12.006 PMID: 16434106.

99. Bai X, Vestal M, Berman R, Negishi M, Spann M, Vega C, et al. Dynamic time course of typical childhood absence seizures: EEG, behavior, and functional magnetic resonance imaging. J Neurosci. 2010; 30(17):5884–93. Epub 2010/04/30. https://doi.org/10.1523/JNEUROSCI.5101-09.2010 PMID: 20427649; PubMed Central PMCID: PMC2946206.

100. Marcus EM, Watson CW. Symmetrical epileptogenic foci in monkey cerebral cortex. Mechanisms of interaction and regional variations in capacity for synchronous discharges. Arch Neurol. 1968; 19(1):99–116. Epub 1968/07/01. https://doi.org/10.1001/archneur.1968.00480010117010 PMID: 4971053

101. Sadleir LG, Farrell K, Smith S, Connolly MB, Scheffer IE. Electroclinical features of absence seizures in sleep. Epilepsy Res. 2011; 93(2–3):216–20. Epub 2011/01/25. https://doi.org/10.1016/j.eplepsyres.2010.12.009 PMID: 21255980.

102. David J, Marathe SB, Patil SD, Wagle GP, Grewal RS. Experimental spike and wave EEG pattern from thalamic stimulation in anaesthetized juvenile monkeys. Indian J Physiol Pharmacol. 1981; 25(3):201–8. Epub 1981/07/01. PMID: 7298144.

103. Falowski SM, Sharan A, Reyes BA, Sikkema C, Szot P, Van Bockstaele EJ. An evaluation of neuroplasticity and behavior after deep brain stimulation of the nucleus accumbens in an animal model of depression. Neurosurgery. 2011; 69(6):1281–90. Epub 2011/05/14. https://doi.org/10.1227/NEU.0b013e3182237346 PMID: 21566538; PubMed Central PMCID: PMC4707959.

104. Cooperrider J, Furmaga H, Plow E, Park HJ, Chen Z, Kidd G, et al. Chronic deep cerebellar stimulation promotes long-term potentiation, microstructural plasticity, and reorganization of perilesional cortical representation in a rodent model. J Neurosci. 2014; 34(27):9040–50. Epub 2014/07/06. https://doi.org/10.1523/JNEUROSCI.0953-14.2014 PMID: 24990924; PubMed Central PMCID: PMC4078081.

105. Bharath RD, Sinha S, Panda R, Raghavendra K, George L, Chaitanya G, et al. Seizure Frequency Can Alter Brain Connectivity: Evidence from Resting-State fMRI. AJNR Am J Neuroradiol. 2015; 36(10):1890–8. Epub 2015/08/22. https://doi.org/10.3174/ajnr.A4373 PMID: 26294642; PubMed Central PMCID: PMC7965029.

106. Baker JL, Ryou JW, Wei XF, Butson CR, Schiff ND, Purpura KP. Robust modulation of arousal regulation, performance, and frontostriatal activity through central thalamic deep brain stimulation in healthy nonhuman primates. J Neurophysiol. 2016; 116(5):2383–404. Epub 2016/09/02. https://doi.org/10.1152/jn.01129.2015 PMID: 27582298; PubMed Central PMCID: PMC5116485.

107. Van Luijtelaar EL, Van der Werf SJ, Vossen JM, Coenen AM. Arousal, performance and absence seizures in rats. Electroencephalogr Clin Neurophysiol. 1991; 79(5):430–4. Epub 1991/11/01. https://doi.org/10.1016/0013-4694(91)90208-I PMID: 1718716.

108. Kimura M, Minamimoto T, Matsumoto N, Hori Y. Monitoring and switching of cortico-basal ganglia loop functions by the thalamo-striatal system. Neurosci Res. 2004; 48(4):355–60. https://doi.org/10.1016/j.neures.2003.12.002 PMID: 15041188.

109. Fridman EA, Beattie BJ, Broft A, Laureys S, Schiff ND. Regional cerebral metabolic patterns demonstrate the role of anterior forebrain mesocircuit dysfunction in the severely injured brain. Proc Natl Acad Sci U S A. 2014; 111(17):6473–8. https://doi.org/10.1073/pnas.1320969111 PMID: 24733913; PubMed Central PMCID: PMC4035959.

110. Mashour GA, Roelfsema P, Changeux JP, Dehaene S. Conscious Processing and the Global Neuronal Workspace Hypothesis. Neuron. 2020; 105(5):776–98. Epub 2020/03/07. https://doi.org/10.1016/j.neuron.2020.01.026 PMID: 32135090.